Crustal-scale structure of South Tien Shan: implications for subduction polarity and Cenozoic reactivation

C. LOURY[1]*, Y. ROLLAND[1], S. GUILLOT[2], A. V. MIKOLAICHUK[3], P. LANARI[4], O. BRUGUIER[5] & D. BOSCH[5]

[1]*Géoazur, Observatoire de la Côte d'Azur, Université de Nice Sophia-Antipolis, 250 rue A. Einstein, 06560 Valbonne, France*

[2]*ISTerre, Université of Grenoble Alpes, CNRS, 1381 rue de la Piscine, 38041 Grenoble, France*

[3]*Institute of Geology, National Academy of Sciences, 30 Erkindyk Ave., Bishkek 720481, Kyrgyzstan*

[4]*Institute of Geological Sciences, University of Bern, Baltzerstrasse 1 + 3, CH3012 Bern, Switzerland*

[5]*Géosciences Montpellier, Université Montpellier II, Place Eugène Bataillon, Batiment 22, 34095 Montpellier, France*

**Corresponding author (e-mail: chloe.loury@geoazur.unice.fr)*

Abstract: Based on new structural and petrological investigations, we present two crustal-scale cross-sections of the Kyrgyz South Tien Shan, and correlations of main faults and units between Kyrgyzstan and China. The overall structure corresponds to a doubly-vergent mountain belt. The Kyrgyz and Chinese areas exhibit identical structural and metamorphic histories. To the west, the Atbashi Range comprises high-pressure oceanic and continental units stacked by north-verging thrusts above a low metamorphic accretionary prism. High-pressure (HP) gneisses are bound to their south by a south-dipping detachment exhibiting mantle relicts. The high-pressure oceanic and continental units underwent similar pressure–temperature (P–T) paths with peak conditions of around 500 °C–20 kbar, followed by rapid exhumation. The overall south-dipping structure and kinematics indicate a south-dipping subduction of the Central Tien Shan Ocean at 320–310 Ma, ending with the docking of the Tarim block to the Kazakh continent. To the east, the Pobeda Massif shows a narrow push-up structure. A major north-vergent thrust exhumes deep-crustal-level granulites, constituting the highest summits, which were thrust towards the north onto low-grade Devonian–Carboniferous schists. The southern part of South Tien Shan is made up of a south-verging thrust stack that formed later during ongoing convergence, reactivated throughout post-30 Ma phases.

The Tien Shan belt extends for more than 2500 km from Uzbekistan to western China. It belongs to the southern part of the Central Asian Orogenic Belt (CAOB), built up by successive continental accretionary events during the Palaeozoic (e.g. Sengör *et al.* 1993; Windley *et al.* 2007; Kröner *et al.* 2014). The South Tien Shan (STS) is an active mountain belt, with summits above 7000 m and large flat areas above 4000 m, which illustrate uplifted peneplains. It is located to the north of the Tarim Basin and the Tibetan plateau (Figs 1 & 2). This active deformation is controlled by reactivated faults inherited from the formation of the CAOB (e.g. Sobel *et al.* 2006*a*; Glorie *et al.* 2011; Macaulay *et al.* 2013, 2014). The STS results from the last accretionary event of the CAOB in Carboniferous time (345–300 Ma), following the successive accretions of the North and Middle Tien Shan in the Lower–Middle Palaeozoic (e.g. Kröner *et al.* 2014). Palaeozoic tectonics and the origin of the STS are still debated, particularly with regard to: (1) the subduction polarity of the Central Tien Shan Ocean; (2) the existence and origin of the STS block; and (3) the localization of the Cenozoic deformation.

Subduction polarity

The vergence of the subduction that led to the closure of the Central Tien Shan Ocean is uncertain and is thought to have been either north-directed (e.g. Windley *et al.* 1990; Allen *et al.* 1992; Biske 1996; Gao & Klemd 2003; Xiao 2004; Zhang *et al.* 2007; Makarov *et al.* 2010; Hegner *et al.*

From: Brunet, M.-F., McCann, T. & Sobel, E. R. (eds) *Geological Evolution of Central Asian Basins and the Western Tien Shan Range*. Geological Society, London, Special Publications, **427**, http://doi.org/10.1144/SP427.4

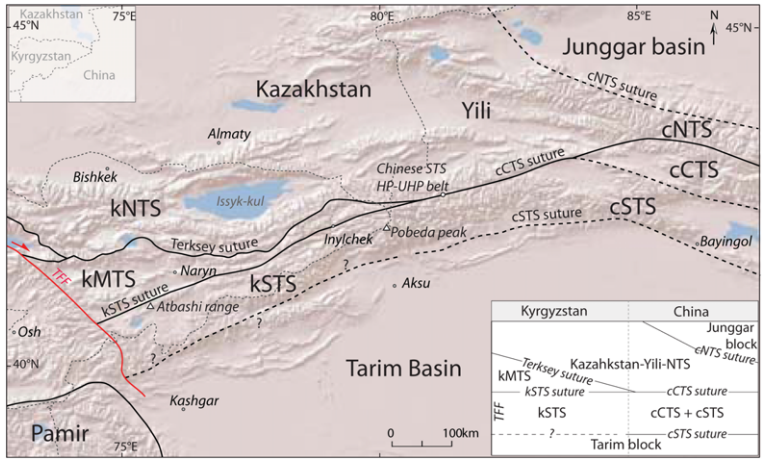

Fig. 1. Tectonic sketch showing the different units distinguished in the Tien Shan and the intervening sutures. Only major boundaries are shown. Compiled from Windley *et al.* (2007) and Charvet *et al.* (2011). (Top-left insert) Sketch map of national boundaries in the study area. (Bottom-right insert) Schematic diagram showing the correspondence of main tectonic units and sutures between the Kyrgyz, Chinese and Kazakh Tien Shan, highlighting the major correlation problems. Abbreviations used: Kyrgyzstan (k): kNTS, Kyrgyz North Tien Shan; kMTS, Kyrgyz Middle Tien Shan; kSTS, Kyrgyz South Tien Shan; TFF, Talas–Fergana Fault; China (c): cNTS, Chinese North Tien Shan; cCTS, Chinese Central Tien Shan; cSTS, Chinese South Tien Shan.

2010; Han *et al.* 2011) or south-directed (e.g. Charvet *et al.* 2007, 2011; Wang *et al.* 2008; Lin *et al.* 2009; Ma *et al.* 2014).

On the *Chinese* side of the belt, the well-studied South Tien Shan high-pressure–ultra-high-pressure belt (the Kekesu, Kebuerte and Akeyazi valleys) preserves eclogite-facies rocks (e.g. Gao & Klemd 2003; Lin *et al.* 2009; Tian & Wei 2013) (Fig. 2). Based on structural, petrological and geochronological data from this metamorphic belt, some authors propose a south-dipping subduction of the Central Tien Shan (CTS) Ocean under the Chinese CTS (CTSc) (e.g. Charvet *et al.* 2007, 2011; Wang *et al.* 2008; Lin *et al.* 2009; Ma *et al.* 2014). This subduction led to the opening of the South Tien Shan Ocean as a back-arc basin between the Tarim block and the CTSc. The subsequent closure of this basin resulted in the formation of the Chinese STS suture (Charvet *et al.* 2007, 2011; Wang *et al.* 2008; Lin *et al.* 2009; Ma *et al.* 2014). This STS suture has only been observed in China but the Central Tien Shan and South Tien Shan as defined in China correspond to the South Tien Shan as described in Kyrgyzstan (e.g. Charvet *et al.* 2011) (Fig. 1). This result makes lateral correlations confusing.

On the *Kyrgyz* side of the STS, several authors proposed that the closure and accretion of the STS occurred due to north-dipping subduction of the Central Tien Shan Ocean below the Middle Tien Shan block during Late Carboniferous times (e.g. Simonov *et al.* 2008; Hegner *et al.* 2010). Furthermore, Alexeiev *et al.* (2007) interpreted the south-dipping structure found in the STS as a formerly top-to-the-south nappe stack, which was overturned in a recumbent fold, resulting in a south-dipping structure.

Origin of the STS

In the Chinese portion of the Tien Shan, the South Tien Shan (STS) and Central Tien Shan (CTS) (i.e. the South Tien Shan in Kyrgyzstan: Fig. 1) were separated from the Tarim block by a back-arc basin. In the Kyrgyz Tien Shan, this back-arc basin and the related suture are not present, or not yet documented. Consequently, the origin of the STS in Kyrgyzstan is also debated: was the STS a distinct tectonic block separated from the Tarim block by a back-arc/oceanic basin as in China? Or does it correspond to the deformed northern rim of the Tarim block, to which it was still attached until the Upper Carboniferous collision? (See, e.g., Hegner *et al.* 2010; Han *et al.* 2011.) Alternatively, Xiao *et al.* (2013) interpreted the STS as a south-verging accretionary complex resulting from a northward subduction of the palaeo-Tien Shan Ocean.

These various models are dependent on the subduction's polarity and on the possible existence of a block drifting in a back-arc position. The geodynamic significance of the STS varies depending on

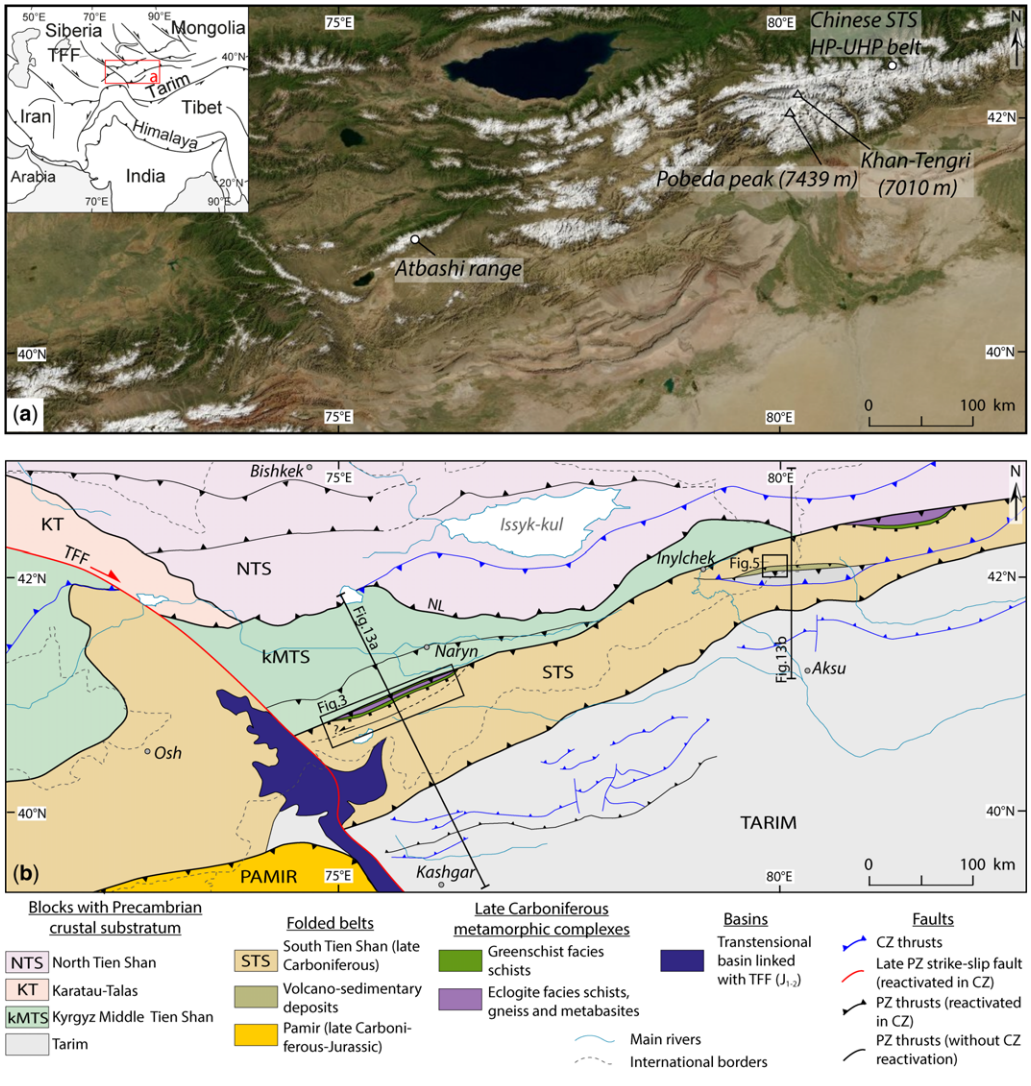

Fig. 2. (**a**) Satellite image of Tien Shan belt showing study areas. (Insert) Geographical situation of Tien Shan in Central Asia (Map data: Google, Image Landsat). (**b**) Tectonic map of Tien Shan (Cenozoic cover removed). The location of detailed maps and the geological crustal-scale cross-sections are shown. Abbreviations used: TFF, Talas–Fergana Fault; NL, Nikolaev Line; STS, South Tien Shan (kSTS + cSTS + cCTS); NTS, North Tien Shan (kNTS + cNTS). Modified after Tursungaziev & Petrov (2008), Wei *et al.* (2009), Chang *et al.* (2012) Macaulay *et al.* (2013).

whether it formed as a drifting unit separated from the Tarim block or as a juvenile block fully constructed during the syn-subduction history.

Localization of Cenozoic deformation and uplift in the STS

Another concern about the formation of the STS is the importance of reactivation of these former Palaeozoic tectonic structures and sutures during Cenozoic deformation of the belt. The last question raised in this paper concerns the role of inherited faults that were reactivated during Cenozoic collisional history. What is the role of newly formed tectonic structures that may explain the crustal-scale geometry of the STS?

To constrain the geological structure and tectonic evolution of the STS, we investigated several transects along the Kyrgyz South Tien Shan range. We conducted detailed studies in the Atbashi Range, the Inylchek Valley and in the Podeda Massif (Fig. 2). The following discussion presents

new crustal-scale geological cross-sections based on both field and published seismic reflection data. We compare them with published data from the Chinese side. These transects provide complementary data on the large-scale structure of the belt and allow us to propose an integrated structural diagram for the South Tien Shan range from the east of the Talas Fergana fault in Kyrgyzstan to western China. Finally, the proposed geodynamic evolution is compared with the previously published numerical model of Vogt & Gerya (2014).

Geological setting

Lateral continuity between China and Kyrgyzstan, and terminology for main geological units

There are some fundamental differences between the terminology used for the main tectonic units in Kyrgyzstan and in China (Fig. 1). In the first, in Kyrgyzstan (k), the Tien Shan belt is divided into three parts: the North Tien Shan (kNTS), the Middle Tien Shan (kMTS) and the South Tien Shan (kSTS). We include the portion of the STS directly south of Kyrgyzstan, in China, as belonging geologically to the kSTS. These three units are separated by two sutures zones: (1) the Terksey suture between the kNTS and kMTS, was formed in the Early Ordovician following the closure of the Terksey Ocean (Lomize *et al.* 1997; Mikolaichuk *et al.* 1997; Burtman 2006), and was later partly reactivated as the Nikolaev Line (Mikolaichuk *et al.* 1995); (2) the kSTS suture, or the Atbashi–Inylchek suture between the kMTS and kSTS, was formed in the Late Carboniferous following the closure of the Central Tien Shan Ocean. It is also referred to as the Turkestan Ocean (Simonov *et al.* 2008; Hegner *et al.* 2010) (Fig. 1).

In China (c), the Tien Shan belt is divided into four parts: the North Tien Shan (cNTS), the Yili block, the Central Tien Shan (cCTS) and the South Tien Shan (cSTS) (Fig. 1). The kMTS has no lateral equivalent in China; in particular, it is not correlated with either the cCTS or the cNTS. The Yili/Tien Shan block is related to the cNTS (Charvet *et al.* 2007; Wang *et al.* 2007, 2008). The cNTS and the Yili block are separated from the cCTS by the cCTS suture zone, formed after the closure of the Central Tien Shan Ocean (also called the Turkestan Ocean or the palaeo-Tien Shan Ocean). The age of this suture is controversial: either Late Devonian–Early Carboniferous (Xiao *et al.* 1992; Gao *et al.* 2000; Gao & Klemd 2003) or Late Carboniferous (Zhang *et al.* 2009; Su *et al.* 2010; Li *et al.* 2011). The cCTS along with the cSTS are equivalent to the kSTS. The cSTS is distinguished from the cCTS because it contains allochtonous units of ophiolites emplaced from the south to the north (Charvet *et al.* 2001, 2007; Laurent-Charvet 2001; Wang *et al.* 2007; Lin *et al.* 2008). In order to clarify this complex terminology, we use the term 'South Tien Shan' to refer to the entire belt comprised of the cCTS, the cSTS and the kSTS. The South Tien Shan is separated from the Tarim block by the cSTS suture. It was formed as a result of the closure of the STS Ocean, which had previously opened in a back-arc setting (Guo *et al.* 2002; Wang *et al.* 2011). Complete closure and formation of the suture is probably Late Devonian–Early Carboniferous in age, slightly younger than the cCTS suture (Zhou *et al.* 2004; Wang *et al.* 2007, 2011). At present, the Chinese cSTS suture does not have a described equivalent in Kyrgyzstan or in the portion of China directly south of Kyrgyzstan. However, a series of small Devonian ophiolite are mapped on the *China Geological Map of Tien Shan* (Hongliang 2007) and could represent the lateral continuity of this suture.

Tectonic history of the STS

The tectonic history of the STS is long and complex. The main structures (1) were formed in Late Carboniferous times and underwent several phases of reactivation from (2) the post-collisional evolution in Permian and Mesozoic times to (3) the Tertiary uplift of the belt, which is still active. The STS suture was formed in the Late Carboniferous following the collision of the Kazakh margin *sensu lato*, comprised of the previously accreted kMTS, Yili block and cNTS, with the Tarim craton. High-pressure rocks related to these sutures are mainly found in two areas: the Atbashi Range in Kyrgyzstan, located just east of the 2000 km-long Talas–Fergana Fault; and the Kebuerte–Kekesu area in western China (Bakirov 1978; Bakirov & Kotov 1988; Tagiri *et al.* 1995; Gao & Klemd 2003; Simonov *et al.* 2008; Hegner *et al.* 2010; Tian & Wei 2013) (Fig. 2). Further east, relicts of ophiolitic mélange are found discontinuously along the cCTS suture (Allen *et al.* 1992; Laurent-Charvet 2001; Guo *et al.* 2002).

Late Palaeozoic tectonics of STS. The ophiolite and metamorphic rocks of the kSTS and cCTS sutures have been investigated in two places separated by approximately 500 km: the Atbashi Range in Kyrgyzstan; and the Kebuerte–Kekesu area in China. In both places, high-pressure rocks had previously been described and the eclogite stage was dated (e.g. Simonov *et al.* 2008; Hegner *et al.* 2010; Su *et al.* 2010; Li *et al.* 2011). The data are consistent with the end of the subduction of the CTS Ocean, and thus the onset of accretion and/or collision

between the Tarim and the Kazakh margin *sensu lato* between 310 and 350 Ma.

In Kyrgyzstan, decimetre-scale lenses of high-pressure rocks crop out in the Atbashi Range (Fig. 2). Bakirov (1978) and Bakirov & Kotov (1988) reported garnet–muscovite schists, with local occurrence of albite and chlorite. Phengite-bearing schists and paragneisses contain lenses of well-preserved eclogites and glaucophane-rich schists. Towards the north, this allochtonous unit overthrusts a dismembered ophiolite (Biske *et al.* 1985; Biske 1996; Alexeiev *et al.* 2007). The conodonts found in the cherts interlayered in the ophiolite constrain its formation age to the Devonian (Frasnian: Alexeiev *et al.* 2007). However, the structural relationships, the kinematics and the significance of these different units are still poorly constrained and can be debated. Concerning the high-pressure rocks, Simonov *et al.* (2008) and Hegner *et al.* (2010) reported pressure–temperature (P–T) conditions of 23–25 kbar and 510–570°C, and 18–24 kbar and 520–600°C, respectively. Simonov *et al.* (2008) obtained a well-constrained $^{40}Ar/^{39}Ar$ age for phengite of 327 ± 4 Ma, and less well-constrained younger ages of between 324 and 182 Ma. This suggests some thermal resetting. Hegner *et al.* (2010) obtained Sm–Nd and $^{40}Ar/^{39}Ar$ ages on an equivalent sample of 319 ± 4 and 316 ± 3 Ma interpreted as crystallization ages related to the high-pressure peak and cooling age, respectively. However, the structural position of the high-pressure unit is still unconstrained because the mafic eclogites were sampled in erratic blocks collected in a Quaternary alluvial fan.

In the Chinese Tien Shan, the structure and evolution of the high-pressure unit is well constrained. The massif is constituted of a stack of units of different metamorphic grade superimposed by top-to-the-north thrusts (Wang *et al.* 2010). This high-pressure unit is thrust on top of low-metamorphic sediments and volcanic rocks. In turn, lower-grade greenschist-facies schists and unmetamorphosed STS sediments are overthrust towards the northern high-pressure unit (Wei *et al.* 2009). As for the degree of metamorphism of the high-pressure unit, a large range of P–T conditions has been obtained spanning 14–28 kbar and 470–600°C (e.g. Gao & Klemd 2003; Gao *et al.* 2008). Ultra-high-pressure conditions are documented in the high-pressure unit by the occurrence of coesite found both in eclogites and the surrounding schists (Yang *et al.* 2011; Lü *et al.* 2008, 2009, 2012; Wei *et al.* 2009). In a more recent study, Tian & Wei (2013) estimated peak pressure conditions at 28–30 kbar and 520–540°C, followed by peak thermal conditions of 540–590°C at a lower pressure of 22–27 kbar. The age of the high-pressure metamorphism in the Chinese high-pressure belt (i.e. peak pressure) is still debated. Gao & Klemd (2003) reported a Sm–Nd isochron age of 343 ± 44 Ma on eclogite, while $^{40}Ar/^{39}Ar$ datings on phengite and crossite (blue amphibole) from blueschists gave ages ranging between 350 and 330 Ma (Xiao *et al.* 1992; Gao *et al.* 2000; Gao & Klemd 2003). However, more recent U–Pb datings on zircon and rutile in eclogites using secondary ion mass spectrometry (SIMS) yield younger ages of 308–321 Ma (Zhang *et al.* 2009; Su *et al.* 2010; Li *et al.* 2011; Liu *et al.* 2014). Similar ages, of approximately 310 and 313–302 Ma, were obtained on phengite in blueschists by $^{40}Ar/^{39}Ar$ and Rb–Sr dating, respectively (Klemd *et al.* 2005). Consequently, these datings show that the last high-pressure event, and thus the ending of the subduction, is no older than 320–310 Ma. Other authors show younger $^{40}Ar/^{39}Ar$ ages (Permian and Triassic) that are ascribed to thermal recrystallization and partial resetting during Permian strike-slip reactivation (de Jong *et al.* 2008; Wang *et al.* 2008).

These two Kyrgyz and Chinese high-pressure massifs, separated by 500 km, show similar ages for high-pressure metamorphism and subsequent cooling. Between these two massifs no occurrence of high-pressure rocks has been documented. Furthermore, the structural and kinematic evolution related to this Late Carboniferous event is still poorly constrained.

Post-collisional evolution of STS. After the Carboniferous collisional event, convergence accommodating the closure of the Palaeotethys Ocean jumped to the south of the Tarim block (e.g. Metcalfe 2013 and references therein). In the CAOB, a transition towards transcurrent deformation along several large equally spaced NW–SE-trending faults occurred (e.g. Talas Fergana Fault). Sinistral strike-slip motion along the ENE-striking STS suture is thought to be contemporaneous with dextral strike-slip movement along the NW–SE-trending Talas Fergana Fault (Alexeiev *et al.* 2007). The Talas Fergana Fault was activated during collision at 312 Ma, but was reactived in the Permian and during Late Triassic–Early Jurassic times (Sobel 1999; Konopelko *et al.* 2013; Rolland *et al.* 2013). During the early Permian phase of transcurrent deformation, the Tarim Basin experienced a strong subsidence (Carroll *et al.* 1995). Intense magmatism affected the Tien Shan belt and the northern Tarim during the early–middle Permian times (290–260 Ma) (e.g. Wang & Liu 1991; Chen *et al.* 1999; S. F. Yang *et al.* 2006; S. F. Yang *et al.* 2007; Chen *et al.* 2009; Li *et al.* 2011; Yu *et al.* 2011; Yu 2009; Biske *et al.* 2013; Zhang & Zou 2013). This magmatism is ascribed by some authors to regional-scale transcurrent tectonics, as suggested by the spatial extent of plutons that are distributed along the

strike-slip faults (e.g. Shu *et al.* 1999; de Jong *et al.* 2008; Wang *et al.* 2009, 2014). However, the alkaline ocean island basalt (OIB)-like geochemistry of the majority of Permian magmatic rocks (e.g. Zhou *et al.* 2009; Zhang *et al.* 2010; Zhang & Zou 2013), together with the large area of magmatism (Yang *et al.* 2005, 2006, 2011), lead other authors to impute this magmatism to mantle plume activity (e.g. Yang *et al.* 2013 and references therein). Finally, Biske *et al.* (2013) suggested that the Permian magmatism in the Tien Shan belt is due to the Tarim plume, but the location of intrusions is controlled by the regional-scale strike-slip tectonic regime. Still, hydrothermal resetting of some zircon ages (Glorie *et al.* 2011) and possible misinterpretations of the metamorphic ages (de Jong *et al.* 2008) may be evidence of such a thermal event.

Mesozoic reactivation of the Tien Shan belt. Ongoing brittle reactivation of the NW-trending Talas Fergana Fault from the Late Triassic to the Early Jurassic is suggested by partial resetting of $^{40}Ar/^{39}Ar$ ages obtained on phengite (Konopelko *et al.* 2013; Rolland *et al.* 2013). This brittle reactivation occurred in a transtensional regime, as suggested on the basis of deformation criteria and the presence of pull-apart basins (Rolland *et al.* 2013). Furthermore, sedimentary deposits and thermochronological data suggest at least one, and up to three, exhumation stages during the Mesozoic (e.g. Hendrix *et al.* 1992; Hendrix 2000; Dumitru *et al.* 2001; De Grave *et al.* 2007, 2011, 2012, 2013; Jolivet *et al.* 2010; Glorie *et al.* 2011; Macaulay *et al.* 2014). This exhumation has generally been interpreted to reflect distal deformation as a result of tectonic accretion along the south Asian margin.

A first exhumation stage occurred during the Late Triassic–Early Jurassic. This was deduced from structural, thermochronological and sedimentary data obtained in the range and in the surrounding basins (e.g. Hendrix *et al.* 1992; Sobel *et al.* 1999; Allen *et al.* 2001; Dumitru *et al.* 2001; De Grave *et al.* 2007, 2011; Jolivet *et al.* 2010; Glorie *et al.* 2011; Macaulay *et al.* 2014). This stage is ascribed to the accretion of the Qiantang block to the southern Eurasian margin at this time (e.g. Yin & Harrison 2000).

A second exhumation stage is suggested during the Late Jurassic–Early Cretaceous (Hendrix *et al.* 1992; Dumitru *et al.* 2001; Jolivet *et al.* 2010; De Grave *et al.* 2013). It may be related to the accretion of the Lhasa block to the Eurasian margin at that time (e.g. Yin & Harrison 2000). However, this phase of exhumation is still subject to debate. Reported Upper Jurassic conglomerates in the South Junggar, the Turpan and the North Tarim basins are attributed to the flexure of the basins as a result of basin-vergent thrusting in the Tien Shan range (Hendrix *et al.* 1992; Hendrix 2000; Li *et al.* 2004). Some apatite fission-track and apatite and zircon (U–Th)/He ages for this period have been reported. Still, it remains unclear whether they can be related to any tectonic event (De Grave *et al.* 2007; Jolivet *et al.* 2010; Glorie *et al.* 2011). Furthermore, from the Late Jurassic to Cretaceous times, a period of thermal stability is well documented, with cooling rates lower than $1\,^{\circ}C\,Ma^{-1}$ (e.g. Bullen *et al.* 2001, 2003; Jolivet *et al.* 2010; Macaulay *et al.* 2014). This long period of tectonic quiescence is also supported by the formation of a large peneplain in the western Central Asia (Vassallo *et al.* 2007; Jolivet *et al.* 2007, 2009; Jolivet, this volume, in press).

The last Mesozoic exhumation phase occurred during Late Cretaceous–Early Palaeogene (Hendrix *et al.* 1992; De Grave *et al.* 2007, 2011, 2012, 2013; Jolivet *et al.* 2010; Glorie *et al.* 2011). Even though Hendrix *et al.* (1992) reported conglomerates in the northern Tarim Basin, this exhumation does not seem to be widespread in the entire Tien Shan range. Indeed, apatite fission-track and apatite (U–Th)/He ages are obtained for these times in the Narat and Bohoro ranges in the Chinese Tien Shan (Jolivet *et al.* 2010). In Kyrgyzstan, similar ages are obtained in intrusions bordering the south Tien Shan suture (Glorie *et al.* 2011), in the Song-Kul Plateau (De Grave *et al.* 2011), in the Issyk-Kul basement (De Grave *et al.* 2013) and in the Altai Mountains (De Grave *et al.* 2012). Macaulay *et al.* (2013, 2014) did not report any evidence of exhumation during the Late Cretaceous in the eastern Kyrgyz Tien Shan. This exhumation phase could be related to accretion of the Kohistan–Ladakh intra-oceanic arc (Hendrix *et al.* 1992; De Grave *et al.* 2007; Jolivet *et al.* 2010) or to the collision of Siberia with the Mongolia–North China block following the closure of the Mongol–Okhotsk Ocean (e.g. Enkin *et al.* 1992; Metelkin *et al.* 2007; Lin *et al.* 2008; Jolivet *et al.* 2010) during Late Cretaceous times.

Cenozoic exhumation. Sedimentary records in the foreland and intramontane basins combined with thermochronological data suggest that the onset of intracontinental deformation in the Tien Shan occurred during Oligocene times, at around 25–20 Ma (e.g. Hendrix *et al.* 1994; Sobel & Dumitru 1997; Yin *et al.* 1998; Bullen *et al.* 2001; Sobel *et al.* 2006*a*, *b*; De Grave *et al.* 2007, 2011; Heermance *et al.* 2008; Glorie *et al.* 2010, 2011; Macaulay *et al.* 2013, 2014; Bande *et al.*, this volume, in press). The onset of deformation is linked to the India–Asia collision, followed by the subsequent transfer of compressional stresses to the Asian continent (e.g. Molnar & Tapponier 1975). A minimal estimation of the exhumation rate during the

Oligocene in the Terksey range of the kMTS is 0.07 ± 0.05 mm a^{-1} (Macaulay *et al.* 2014).

An increase of the exhumation rate occurred during Miocene times (15–5 Ma). This is suggested by an increase in cooling rates deduced from the thermochronological data (e.g. Bullen *et al.* 2001; Sobel *et al.* 2006*b*; De Grave *et al.* 2007, 2011; Heermance *et al.* 2008; Glorie *et al.* 2010, 2011; Macaulay *et al.* 2013, 2014). The exhumation rate is estimated at 0.1–0.4 mm a^{-1} in the Terksey range (Macaulay *et al.* 2013). This increase in the exhumation rate is also suggested by the magnetostratigraphic data and sedimentary records (e.g. Abdrakhmatov *et al.* 1996; Charreau *et al.* 2006). A shortening event in the entire Tien Shan at that time is thus suggested (Sobel *et al.* 2006*b*), which could be explained by a delamination of the lithosphere under the Tien Shan (Li *et al.* 2009).

An acceleration of the exhumation is evidenced in the Pliocene (3–2 Ma) by thermochronological, magnetostratigraphic and sedimentary data (e.g. Fortuna *et al.* 1994; Abdrakhmatov *et al.* 2001; Bullen *et al.* 2001, 2003; Glorie *et al.* 2011; Macaulay *et al.* 2014). An acceleration of the denudation of the modern Tien Shan range could explain this increase in exhumation rates (De Grave *et al.* 2007). This exhumation is ongoing and coupled with climatic stress, which explains the Tien Shan landscape and, particularly, summits above 7400 m in the Pobeda Massif. However, it is uncertain whether this increase in denudation reflects a tectonic component or is solely a reflection of climatic influences.

The Cenozoic deformation of the Tien Shan, however, seems to be out of sequence (Jolivet *et al.* 2010; Macaulay *et al.* 2014). This out-of-sequence activation could be explained by the dip and nature of the inherited structures, which are more or less susceptible to reactivation (e.g. Macaulay *et al.* 2014).

Origin of the STS basement

As described above, the STS underwent a complex tectonic and metamorphic evolution from its main tectonic stage at approximately 310–320 Ma to the ongoing uplift. A significant uncertainty remains regarding the nature and origin of the STS basement. It is unclear whether the STS was a distinct tectonic block or if it corresponds to the northern margin of the Tarim block. The STS basement is unknown in Kyrgyzstan. Sedimentary series in the STS are Silurian–Carboniferous in age (e.g. Tursungaziev & Petrov 2008), and are cross-cut by Upper Carboniferous–Lower Permian granitoid intrusions. Their emplacement is related to Tarim–CAOB collisional or post-collisional processes (e.g. Biske *et al.* 2013). The U–Pb ages of zircons from these granites yield 295–292 Ma (Konopelko *et al.* 2007, 2009) and 302–288 Ma (Glorie *et al.* 2011). Therefore, the age of STS sedimentary series and of cross-cutting intrusions is well known but the age, and thus the origin, of the STS basement remain unknown.

Geological mapping and cross-sections along Kyrgyz STS

The Atbashi Range

Although the rocks outcropping in the Atbashi Range have been described previously, the structure of the range remains poorly constrained (Bakirov 1978; Biske *et al.* 1985; Bakirov & Kotov 1988; Biske 1996; Alekseev *et al.* 2007; Hegner *et al.* 2010). New field investigations allow us to distinguish three different structural units, which are ascribed to different parts of a preserved subduction prism (see also Loury *et al.* 2013) (Figs 3–5):

- An accretionary prism featuring a tectonic mélange composed of a sedimentary matrix that includes metric to decametric slices of serpentinites and metabasalts. This mélange was overprinted by greenschist-facies metamorphism and thus represents the shallow part of the accretionary prism. An unmetamorphosed dismembered ophiolite thrusts towards the north on top of the accretionary prism (Fig. 5a). This ophiolite is made up of pillow-basalts and flaser gabbros (Fig. 5b), with peridotite nodules, serpentinites, siliceous cherts and plagiogranites covered by limestones. This ophiolite is a remnant of fragments of oceanic lithosphere thrust onto the low-grade sediments before the final emplacement of high-pressure units during the Upper Carboniferous.
- A high-pressure–low-pressure complex is thrust towards the north over a shallow accretionary prism. It is divided into two units:
  - The first unit is a sedimentary mélange several hundreds of metres thick, with occurrences of jadeite and garnet (Fig. 5e, f). Decametre-scale mafic eclogite boudins are incorporated into this mélange (Fig. 5c, d), which records eclogite-facies metamorphic conditions. Observations lead to us to argue that this unit may constitute the deep part of the subduction prism.
  - The second unit of the high-pressure–low-temperature complex is a continental unit thrust towards the north over the sedimentary mélange. It is made of folded ortho- and paragneisses. Observations show evidence for retrogression during the blueschist and greenschist facies metamorphic stages (Fig. 5g).

  The high-pressure–low-temperature complex is separated from the upper part of the subduction

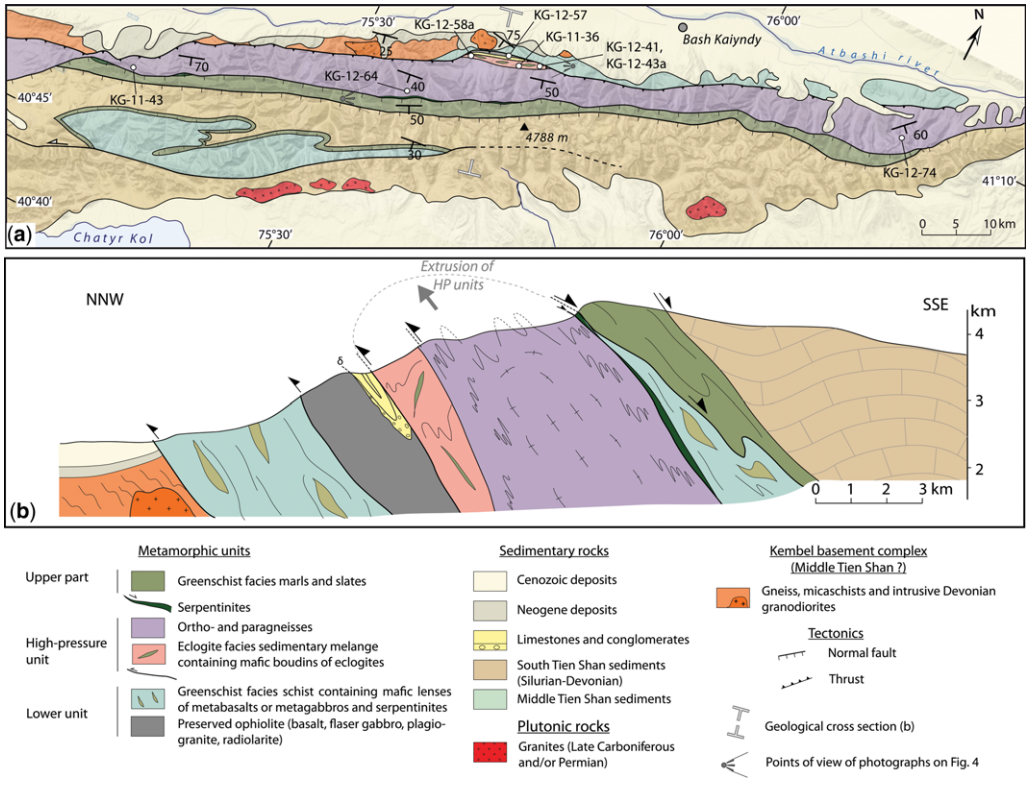

Fig. 3. (**a**) Geological map of the Atbashi Range with the location of the samples described in the text. GPS coordinates are presented in Tables 1 & 4. Modified after Tursungaziev & Petrov (2008). (**b**) Cross-section of the Atbashi Range.

prism by a top-to-the-south detachment along which serpentinites are found.

- The upper part of the subduction prism is made of two sedimentary units:
  - The first unit is made up of marls and slates metamorphosed under greenschist-facies conditions. Shear-sense criteria indicates top-to-the-south shearing (Fig. 5h).
  - The second unit is made of unmetamorphosed Silurian–Carboniferous limestones and marls. These two units could represent two different crustal levels within the Tarim platform.

In this area, the crystalline basement is not exposed. Within this upper section, a major east–west-trending vertical fault exhibiting horizontal striae is observed to the west of the range in the

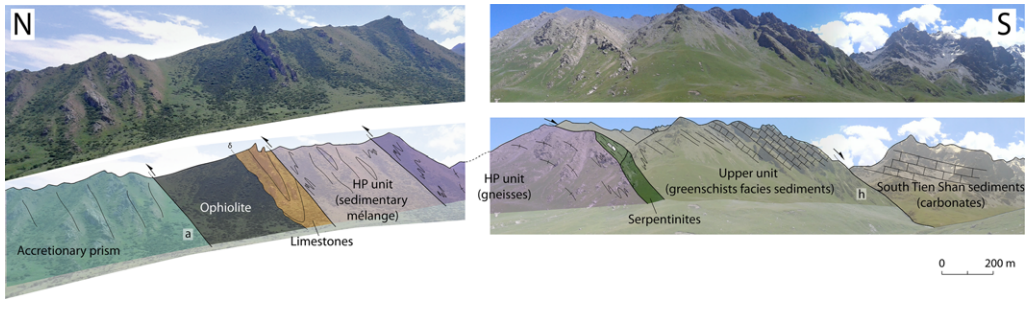

Fig. 4. Panoramic photograph of the Atbashi Range and interpretation. The point of view of the photographs is shown in Figure 3. Letters in boxes indicate the location of kinetic criteria photographs in Figure 5.

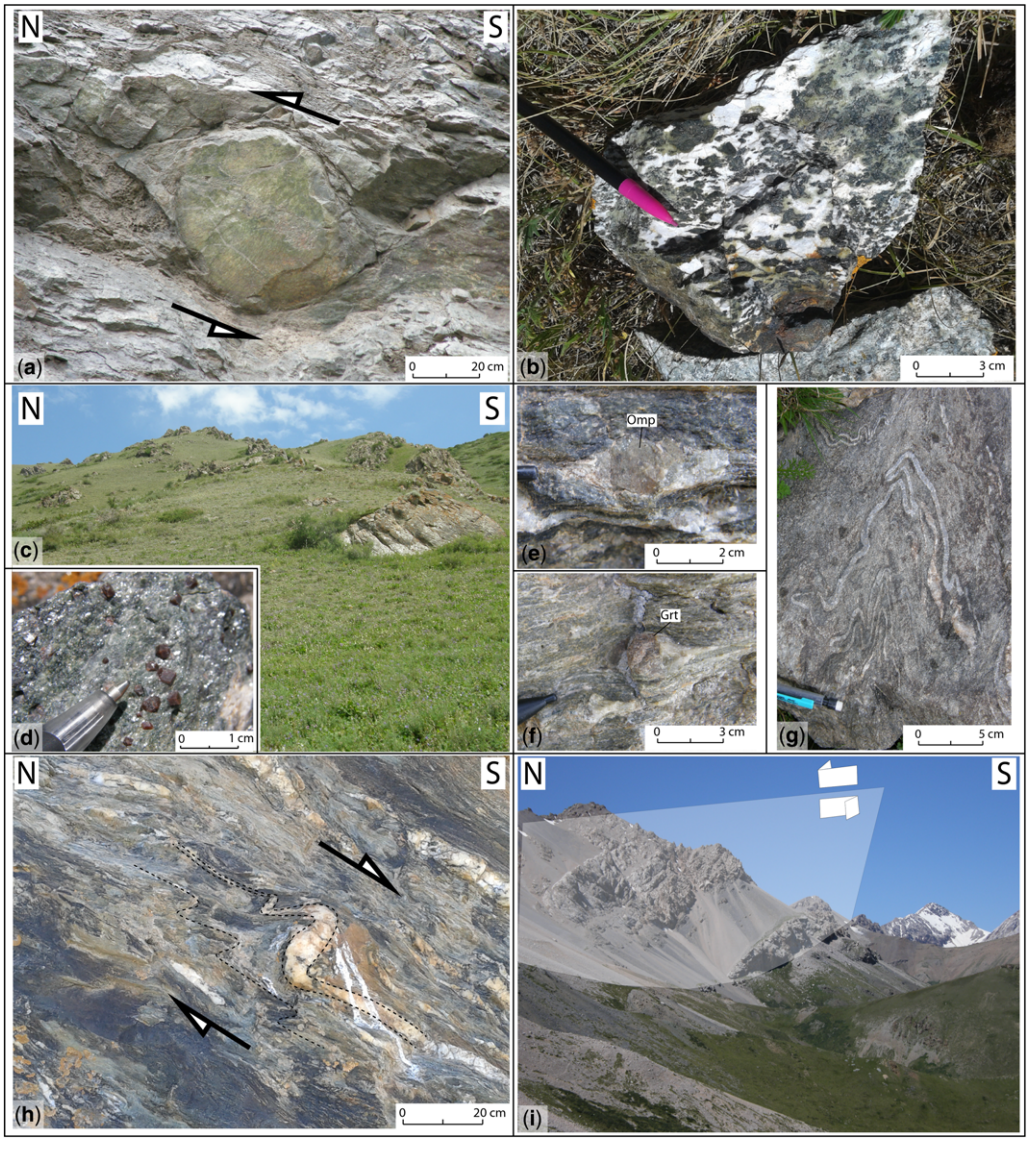

Fig. 5. Field photographs of Atbashi Range. (**a**) Block of greenschist-facies metabasite in the shallow accretionary prism, showing top-to-the-north sense of shear, consistent with thrusting motion of the ophiolite on top of the greenschist-facies accretionary prism. (**b**) Flaser-gabbro showing hornblende corona around magmatic pyroxene, with a slight greenschist-facies overprint. These characteristics are typical of ductile deformation of mid-oceanic ridges. (**c**) Prominent boudins of outcropping mafic eclogites within a soft metasedimentary matrix (which is covered by grassy vegetation) in the metasedimentary mélange of high-pressure unit. (**d**) Sample of mafic eclogite showing euhedral millimetre-scale garnet, omphacite and phengite, collected from the sedimentary mélange of the high-pressure unit. (**e**) Centimetre-scale omphacite (Omp) and (**f**) garnet (Grt) in the sedimentary mélange of the high-pressure unit. (**g**) Quartz veins showing multiple folding phases in a paragneiss of the continental high-pressure unit. (**h**) Quartz veins exhibiting drag folds with top-to-the-south sense of shear in greenschist-facies metasediments of the upper unit, consistent with a top-to-the-south detachment of the upper unit above the high-pressure unit. (**i**) View to the west of the strike-slip fault in the carbonates of the upper unit.

Tash Rabat Valley (Fig. 5i). The motion on this fault is thought to be sinistral, but no clear kinematic criteria have been found.

The Pobeda Massif

The most prominent feature of the Pobeda Massif is a major top-to-the-north thrust, referred to as the Pobeda Thrust, which bounds the northern flank and crest line of the Pobeda Peak (Figs 6 & 7a). This thrust is responsible for the uplift of deep crustal (basement) levels, exhibited by granulite-facies clino- and ortho-pyroxene-bearing gneisses and marbles, previously mapped as syenites (Mikolaichuk & Buchroithner 2008; Tursungaziev & Petrov 2008). The paragneisses are migmatized and alternate with coarse-grained granulites *sensu stricto*, which appear to be the residue of intense migmatization (Fig. 7b). Their composition is Al–K–Fe-rich, highlighted by the abundance of orthoclase and pyroxene (Fig. 8), in agreement with a charnockitic protolith (Newton 1992). Ages of the protolith and the metamorphism are unknown. Thin-section textural relationships between the different minerals imply that they represent a high-temperature equilibrium (triple-joints, myrmekites) (Fig. 8). The main granulite-facies metamorphic paragenesis is made up of pyroxenes + K-feldspar + plagioclase + quartz ± spinel (Fig. 8). This high-temperature paragenesis is partially retrogressed into the amphibolite facies, as shown by hornblende overgrowths of pyroxenes. The co-stability of clino- and orthopyroxene suggests a minimum temperature of 800°C (e.g. Wells 1977). These high-grade deep-crustal rocks are thrust towards the north over shallower levels made of black schists, sandy limestones and metabasites (metabasalts and metagabbros) metamorphosed at greenschist-facies conditions (Fig. 7f). The age of this formation is supposed to be Devonian–Carboniferous (Tursungaziev & Petrov 2008; Mikolaichuk & Buchroithner 2008). It is thought to be the lower part of the sedimentary series of the STS. This greenschist-facies volcanosedimentary series could be the lateral continuation of similar greenschist-facies rocks observed in the Atbashi Upper Unit (see the previous subsection on 'The Atbashi Range'). In the Pobeda Massif, this unit is thrust towards the north over the less metamorphosed Devonian–Carboniferous STS sedimentary series (Mikolaichuk & Buchroithner 2008; Tursungaziev & Petrov 2008). This lower unit is intruded by late Carboniferous calc-alkaline granite (Tursungaziev & Petrov 2008) (Fig. 7c). In the central part of this intrusion, the granite exhibits mixing between the most mafic mantle-derived components and a mesocratic crustal-derived component. The mineral assemblage is plagioclase + amphibole + biotite (Fig. 7e). At the intrusion rims, its composition evolves towards a leucocratic composition featuring K-feldspar + quartz + tourmaline (Fig. 7d). We speculate that the age of regional metamorphism is Carboniferous and is contemporaneous with granite emplacement (Tursungaziev & Petrov 2008). However, this hypothesis remains to be tested.

A complementary cross-section was made 30 km to the west, near Inylchek village. There, a north-verging thrust places the Palaeozoic series above deposits of a Tertiary basin (Fig. 7g). Basin strata are deposited on top of a flat basement surface, which is interpreted as a Jurassic–Cretaceous peneplain (e.g. Jolivet *et al.* 2007). We interpret this thrust as the lateral continuity of the major Pobeda Thrust, as suggested by cartography and aerial images.

Petrology of the Atbashi Range and comparison with the Chinese STS

Major and trace element compositions were acquired on both unmetamorphosed basalt from the ophiolite and mafic eclogites from the sedimentary mélange. ICP-OES (inductively coupled plasma optical emission spectrometry) and ICP-MS (inductively coupled plasma mass spectrometry) analyses were performed at the CRPG Nancy (Table 1). Local mineral compositions were determined using a Cameca SX100 electron probe microanalyser (EPMA) at the Geosciences Laboratory in Montpellier and at the Grenoble ISTerre Laboratory (Tables 2–4). The analytical settings used for timely analyses were 20 keV and 10 nA. Laser ablation analyses (Table 5) were conducted using a Geolas platform housing a 193 nm CompEx 102 laser from LambdaPhysik, which was connected to an Element XR ICP-MS from ThermoFinnigan at Géosciences Montpellier UMR5243-CNRS (France). Details of the analytical procedure are described in Bruguier *et al.* (2009) and Bosch *et al.* (2011).

Geochemistry of metabasalts

The basalt and the mafic eclogite from the Atbashi Range provide similar geochemical results. Analyses exhibit compositions with strong N-MORB (normal-type mid-ocean ridge basalt) affinities, depleted in LILEs (large ion lithophile elements) and LREE (light rare earth elements) with respect to HFSEs (high field strength elements) (Fig. 9). With respect to typical N-MORB tendencies (Sun & McDonough 1989), both rock types are enriched up to 30 times more in Cs, Rb, Ba and U, and to a lesser extent in Sr and Pb. Th is almost identical to

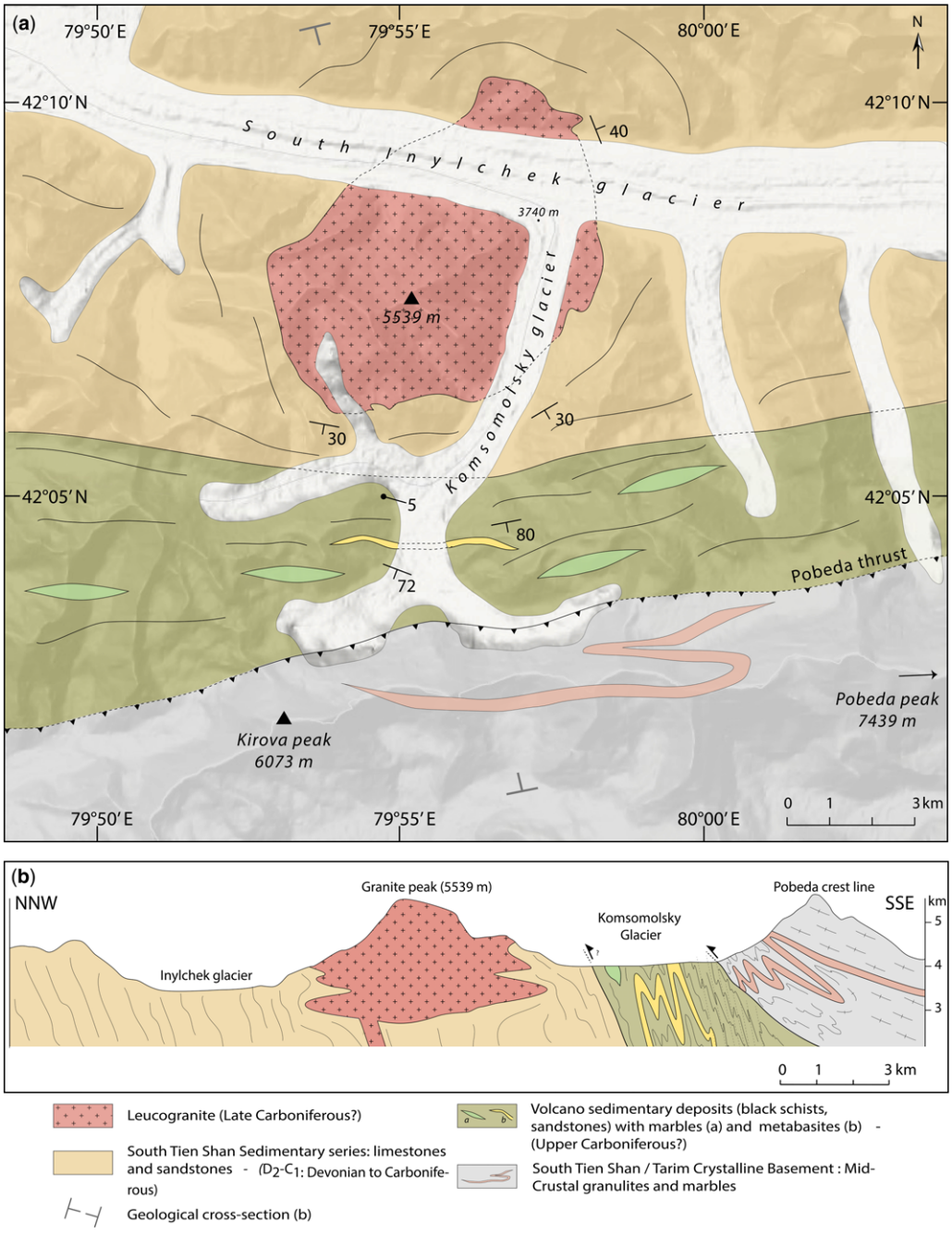

Fig. 6. Geological map (**a**) and cross-section (**b**) of Pobeda Massif. Modified after Mikolaichuk & Buchroithner (2008) and Tursungaziev & Petrov (2008).

typical N-MORB. This pattern demonstrates the oceanic origin of mafic eclogites, in agreement with Simonov *et al.* (2008) and Hegner *et al.* (2010). The relative immobility of Th and the increasing mobility of lighter LILEs suggest that intense seafloor hydrothermal alteration is still

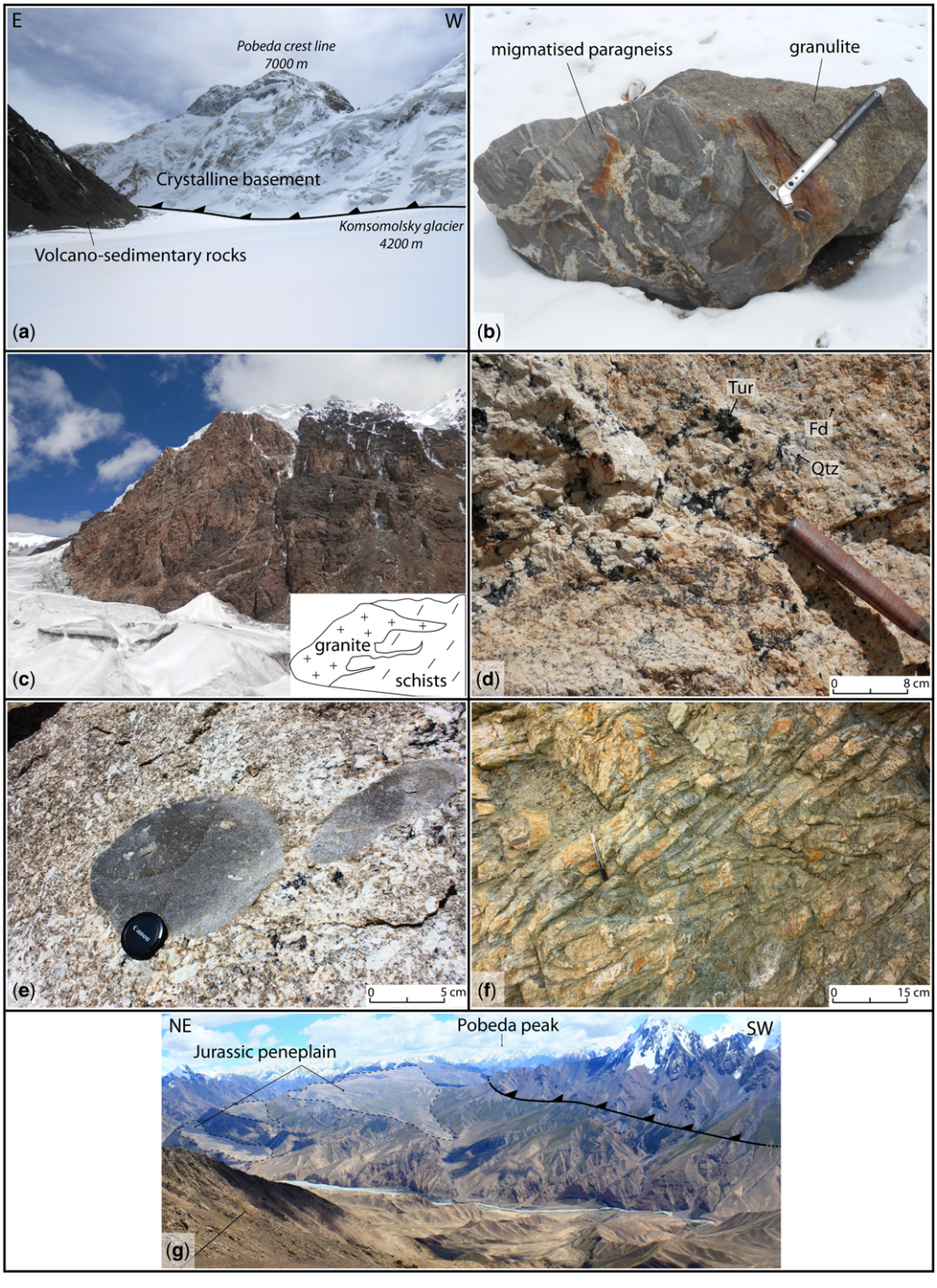

Fig. 7. Field photographs of the Pobeda Massif. (**a**) Top-to-the-north thrust (Pobeda Thrust) of Pobeda crystalline basement over the volcano-sedimentary rocks of presumed Carboniferous age, according to the *Geological Map of Kyrgyzstan* (Tursungaziev & Petrov 2008). (**b**) Block of granulite-facies rocks showing the relationship between the migmatized paragneisses and the granulite *sensu stricto*. (**c**) Kilometre-scale granite intrusion in the Devonian–Carboniferous sediments of the STS. (**d**) Tourmaline (Tur), feldspar (Fd), quartz (Qtz)-rich leucocratic granite from the

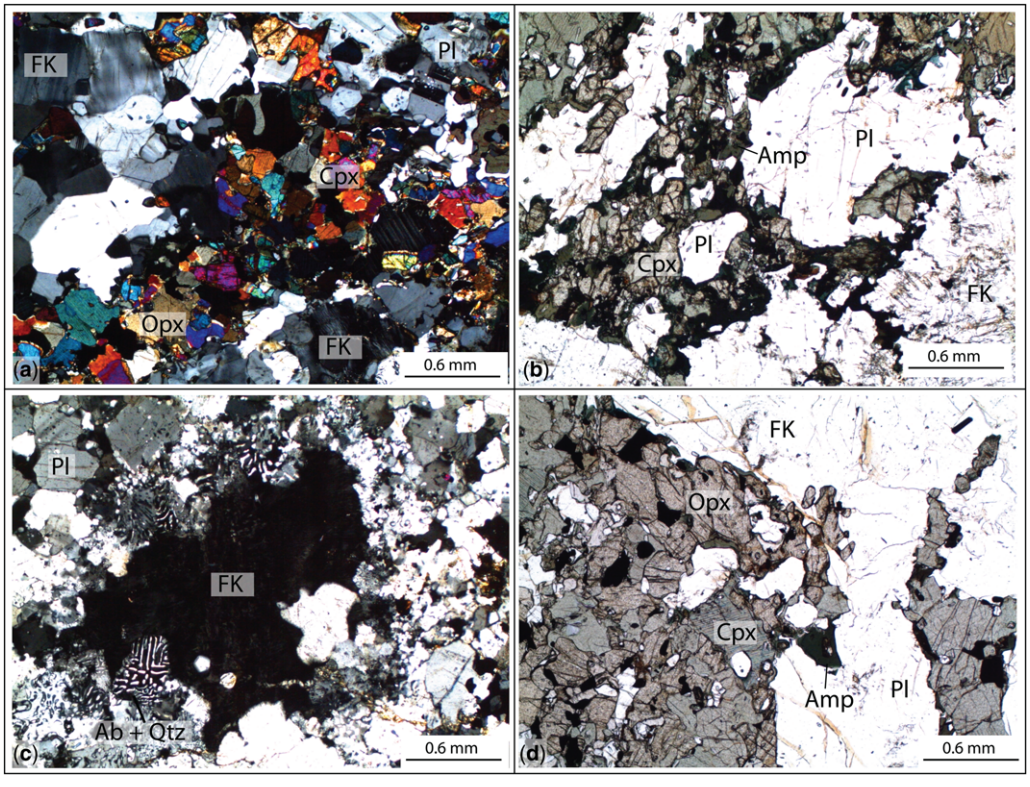

Fig. 8. Microphotographs of the granulites from the Pobeda Massif. (**a**) Clinopyroxene (Cpx), orthopyroxene (Opx), plagioclase (Pl) and K-feldspar (FK) showing a textural equilibria with triple-junctions (plane polarized light). (**b**) Amphibole (Amp) overgrowths over clinopyroxene (Cpx) indicating a partial retrogression (plane polarized light). (**c**) K-Feldspar surrounded by myrmekite (intergrowth between quartz (Qtz) and albite (Ab)) typical of high-temperature conditions (crossed polars). (**d**) Association of orthopyroxene (Opx) and clinopyroxene (Cpx) with a few amphibole (Amp) overgrowths.

preserved in the eclogite sample. This hydrothermal imprint, combined with the presence of flaser gabbros and serpentinites in the ophiolite, argues for a slow spreading-ridge setting (e.g. Lagabrielle & Cannat 1990).

Pressure–temperature conditions of mafic eclogites

Mineralogy. A mafic eclogite sampled in a boudin within the high-pressure sedimentary mélange has been studied to unravel the P–T path of the high-pressure mélange unit (Fig. 10a). This eclogite is made of garnet porphyroblasts (*c.* 50% mode) surrounded by a matrix containing omphacite (*c.* 45%) and rutile (*c.* 3%), with glaucophane and zoisite in minor proportion. Millimetre-size garnet porphyroblasts contain a high proportion of inclusions (up to 40%) of omphacite, quartz, rutile, glaucophane and, in some occurrences, phengite (Fig. 10b). Quartz inclusions form a corona in the garnet mantle. The garnet end-member proportions vary from core to rim, indicating a growth-related chemical zoning (Fig. 10c). From the core to the rim, almandine

Fig. 7. *(Continued)* rim of the intrusion, showing a more differentiated composition than in the central part of the intrusion. (**e**) Mesocratic granite from the central part of the intrusion, with rounded enclaves of a fine-grained dioritic (amphibole + plagioclase) composition. This more mafic calc-alkaline component may reflect a mantle source, which interacted and mixed with a crustal component. (**f**) Volcano-sedimentary rocks showing folded alternations of dark schists (comprising metavolcanics and metagabbros) and yellow sandy limestones. The whole unit was metamorphosed under the greenschist facies (actinolite–epidote–chlorite–sericite). (**g**) Picture of the same thrust as in picture (a), 30 km to the west in Inylchek area. Here, the Tertiary basin, deposited above the Jurassic peneplain, is folded and overthrust by the top-to-the-north Pobeda Thrust.

Table 1. *Chemical composition of mafic eclogites from a boudin in the sedimentary mélange of the high-pressure unit (samples KG-12-41 and KG-12-43a) and basalt (sample KG-12-57) from the ophiolite*

	Mafic eclogite		Basalt
Sample name Sample coordinates	KG-12-41 N 41° 02′ 28.8″, E 75° 43′ 15.1″	KG-12-43a N 41° 02′ 28.8″, E 75° 43′ 15.1″	KG-12-57 N 41° 01′ 58.3″, E 75° 40′ 13.3″
Major elements			
SiO_2	45.79	48.60	46.01
Al_2O_3	16.85	13.00	15.50
Fe_2O_3	10.66	10.82	9.49
MnO	0.20	0.16	0.14
MgO	4.67	8.85	5.51
CaO	14.06	8.44	7.27
Na_2O	2.04	4.30	5.94
K_2O	0.70	0.53	0.11
TiO_2	0.83	0.75	0.93
P_2O_5	0.07	b.d.	0.10
LOI	3.37	3.56	8.61
Total	99.23	99.03	99.61
Trace elements			
As	b.d.	3.60	3.84
Ba	36.52	156.00	17.55
Be	b.d.	0.71	b.d.
Bi	b.d.	b.d.	b.d.
Cd	b.d.	b.d.	b.d.
Ce	3.72	3.73	4.12
Co	38.85	43.14	45.36
Cr	447.50	206.00	447.30
Cs	1.14	1.21	0.27
Cu	83.93	65.34	174.80
Dy	3.34	2.59	3.97
Er	2.12	1.69	2.56
Eu	0.69	0.45	0.78
Ga	15.90	12.53	15.72
Gd	2.63	1.82	3.13
Ge	1.75	1.64	1.16
Hf	1.14	1.03	1.27
Ho	0.71	0.57	0.87
In	0.08	b.d.	0.07
La	1.00	1.34	1.29
Lu	0.35	0.28	0.41
Mo	3.50	3.09	2.56
Nb	0.73	1.69	0.56
Nd	3.85	3.51	5.04
Ni	94.51	92.61	145.20
Pb	1.20	2.74	4.15
Pr	0.59	0.61	0.77
Rb	14.90	15.86	1.79
Sc	49.54	51.03	39.52
Sb	0.67	b.d.	0.39
Sm	1.68	1.22	2.03
Sn	0.55	0.60	0.59
Sr	134.70	43.18	77.03
Ta	0.06	0.09	0.05
Tb	0.48	0.36	0.58
Th	0.09	0.11	0.07
Tm	0.32	0.26	0.39
U	0.09	0.06	0.09
V	221.80	241.10	227.60

(*Continued*)

Table 1. *Continued*

	Mafic eclogite		Basalt
Sample name Sample coordinates	KG-12-41 N 41° 02′ 28.8″, E 75° 43′ 15.1″	KG-12-43a N 41° 02′ 28.8″, E 75° 43′ 15.1″	KG-12-57 N 41° 01′ 58.3″, E 75° 40′ 13.3″
W	3.37	3.06	2.59
Y	19.56	15.83	24.85
Yb	2.23	1.79	2.60
Zn	65.67	101.40	83.09
Zr	36.65	33.46	40.38

b.d., below detection.
Major elements in wt%; trace elements in ppm.
Samples are located in Figure 3a.

content decreases ($Alm_{70\rightarrow50}$), pyrope content increases ($Pyr_{10\rightarrow27}$), and grossular content slightly decreases from core to mantle ($Grs_{21\rightarrow18}$) and then increases ($Grs_{18\rightarrow27}$). The jadeite content in omphacite inclusions increases from the garnet core to the quartz-rich corona in the garnet mantle ($Jd_{31\rightarrow35}$). The jadeite content decreases towards the rim ($Jd_{35\rightarrow25}$) and is the same as the outer rim

Table 2. *Representative electron microprobe chemical analyses (in oxide wt%) and structural formulae (in p.f.u.) for minerals of a mafic eclogite from a boudin in the sedimentary mélange of the high-pressure unit and basalt (sample KG-11-36, N 41° 02′ 0,43″ E 75° 42′ 17,18″, located on Fig. 3a)*

	Garnet				Omphacite			Phengite	Glaucophane	
	core	mantle	rim		Inc. in grt core	Inc. in grt mantle	Matrix	Inc. in grt core		Inc. in grt core
SiO_2	37.91	38.11	38.77		53.57	54.33	54.68	49.19		49.19
TiO_2	0.08	0.08	0.06		0.11	0.05	0.05	0.34		
Al_2O_3	21.96	22.16	23.21		7.07	7.87	6.26	28.21		
FeO	28.87	29.23	23.28		13.50	14.45	7.49	4.72		
MnO	0.78	0.60	0.23		0.03	0.05	0.04	0.01		
MgO	2.58	2.83	7.28		5.28	4.22	10.75	2.48		
CaO	8.30	8.35	7.99		9.37	8.02	15.20	0.07		
Na_2O	b.d.	b.d.	b.d.		8.84	9.78	5.93	0.66		
K_2O	b.d.	b.d.	b.d.		b.d.	b.d.	b.d.	10.82		
Total	100.48	101.36	100.82		97.77	98.77	100.40	96.47		
O = 12				O = 6				O = 11	O = 23	
Si	2.98	2.97	2.95		2.00	2.00	1.99	3.31		7.90
Ti	0.00	0.01	0.00		0.00	0.00	0.00	0.00		0.01
Al	2.04	2.01	2.08		0.32	0.35	0.27	2.24		1.43
Mn	0.05	0.04	0.02		0.00	0.00	0.00	0.00		0.02
Mg	0.30	0.33	0.83		0.30	0.24	0.58	0.25		2.00
Ca	0.70	0.69	0.65		0.38	0.32	0.59	0.00		0.18
Na	–	–	–		0.65	0.71	0.42	0.09		1.87
K	–	–	–		–	–	–	0.93		0.01
Fe^{2+}	1.90	1.88	1.48		0.09	0.09	0.06	0.27		1.12
Fe^{3+}					0.34	0.37	0.16			0.52
X_{pyr}	0.10	0.12	0.27	X_{hed}	0.09	0.09	0.06		$(Na + K)_A$	0.05
X_{alm}	0.64	0.64	0.50	X_{acm}	0.34	0.36	0.17		Na_B	1.82
X_{sps}	0.02	0.01	0.01	X_{jd}	0.32	0.35	0.25			
X_{grs}	0.24	0.23	0.22	X_{di}	0.3	0.24	0.58			

Abbreviations used: $X_{pyr,\ alm,\ sps,\ grs}$, proportions of pyrope, almandine, spessartine and grossular (end members) in garnet; $X_{hd,\ acm,\ jd,\ di}$, proportions of hedenbergite, acmite, jadeite and diopside (end members) in clinopyroxene; inc. in grt, inclusions in garnet; b.d., below detection; $(Na + K)_A$, Na + K on crystalline site 'A' in amphibole; Na_B, Na on crystalline site 'B' in amphibole.
Fe^{3+} estimated using the proportion of the acmite end member for omphacite.
Fe^{3+} estimated using the method of Holland & Blundy (1994) for glaucophane.

Table 3. *Representative electron microprobe chemical analyses (in oxide wt%) and structural formulae (in p.f.u.) for garnet, omphacite and phengite of a metasedimentary eclogite from the sedimentary mélange of the high-pressure unit (sample KG-12-58a, N 41° 1′ 27.75″, E 75° 40′ 18.27″, located in Fig. 3a)*

	Garnet		Omphacite		Phengite	
SiO_2	37.63	38.19	56.73	56.24	51.58	51.95
TiO_2	0.06	0.14	0.02	0.03	0.13	0.20
Al_2O_3	21.78	21.68	11.13	10.99	29.18	27.54
FeO	25.23	25.38	6.54	6.05	1.53	2.47
MnO	1.79	1.93	0.04	0.05	0.03	0.04
MgO	1.63	1.62	6.97	6.60	3.75	3.66
CaO	12.36	12.06	11.41	11.99	0.02	0.04
Na_2O	b.d.	b.d.	8.01	7.82	0.63	0.27
K_2O	b.d.	b.d.	b.d.	b.d.	9.81	9.99
Total	100.48	101.00	100.84	99.77	96.66	
O = 12		O = 6		O = 11		
Si	2.97	2.99	2.00	2.00	3.36	3.42
Ti	0.00	0.01	0.00	0.00	0.00	0.01
Al	2.02	2.00	0.47	0.46	2.25	2.14
Mn	0.12	0.13	0.00	0.00	0.00	0.00
Mg	0.19	0.19	0.37	0.35	0.14	0.36
Ca	1.04	1.01	0.43	0.46	0.08	0.00
Na	–	–	0.55	0.54	0.21	0.04
K	–	–	–	–	0.78	0.84
Fe^{2+}	1.66	1.66	0.11	0.10	0.15	0.14
Fe^{3+}			0.09	0.08		
X_{pyr}	0.06	0.06				
X_{alm}	0.55	0.56				
X_{sps}	0.04	0.04				
X_{grs}	0.35	0.34				
X_{hed}			0.11	0.10		
X_{acm}			0.09	0.08		
X_{jd}			0.47	0.47		
X_{di}			0.37	0.35		

Abbreviations used: $X_{pyr, alm, sps, grs}$, proportions of pyrope, almandine, spessartine and grossular (end members) in garnet; $X_{hd, acm, jd, di}$, proportions of hedenbergite, acmite, jadeite and diopside (end members) in clinopyroxene; inc., inclusions; b.d., below detection. Fe^{3+} estimated using the proportion of acmite end member.

in the matrix (Jd_{25}). The few glaucophane occurrences are in the matrix and as inclusions at the core of garnet. Phengite only occurs in the core of garnet. Some quartz inclusions have radial fractures in the surrounding garnet but coesite was not detected by Raman analyses. Rutile occurs as inclusions in garnet and in the matrix, often surrounded by a retrograde ilmenite corona. This distribution of mineral inclusions in garnet indicates two events: (1) prograde zoning from the core to the mantle, suggested by the occurrence of glaucophane in the garnet core and the increasing jadeite content in the omphacite up to the mantle; and (2) subsequent retrogression recorded from the mantle to the rim.

P–T conditions. Garnet crystallization started during the prograde stage, as suggested by the presence of glaucophane and omphacite with a low jadeite content. Garnet–omphacite thermometry (Ravna 2000) and garnet–omphacite–phengite geobarometry (Waters & Martin 1993; Waters 1996) indicate *P–T* conditions for crystallization of the garnet core at 450 ± 50°C and 17 ± 2 kbar (Fig. 11). The maximum jadeite content (Jd_{35}) in omphacite is observed for inclusions located close to the quartz corona. This suggests that this part of the grain crystallized at peak pressure conditions. The quartz inclusions in the corona may be explained by an excess of Si in the bulk composition at this stage. The absence of phengite in equilibrium with this omphacite prevents the use of garnet–omphacite–phengite geobarometery. Garnet–omphacite thermometry (Ravna 2000), taking into consideration previous pressure estimates of Simonov *et al.* (2008) (23–25 kbar) and Hegner *et al.* (2010) (18–24 kbar), indicates temperatures of 505 and 535°C for pressure of 18 and 25 kbar, respectively (Fig. 11). Zr-in-rutile thermometry (Ferry & Watson 2007) indicates temperatures of 510 ± 25°C (Table 5). The radial fractures around quartz are ascribed to decompression of a

Table 4. *Representative electron microprobe chemical analyses (in oxide wt%) and structural formulae for phengite (in pfu) of gneisses from continental* high-pressure *unit (samples KG-11-43, KG-12-64 and KG-12-74)*

	Phengite		
Sample name Sample coordinates	KG-11-43 N40°52′44.88″, E75°15′59.04″	KG-12-64 N40°56′20.6″, E75°34′25.6″	KG-12-74 N41°06′28.0″, E75°58′29.6″
SiO_2	51.56	50.72	49.84
Al_2O_3	25.87	28.07	27.41
FeO	2.53	2.77	3.98
MnO	0.00	0.02	0.06
MgO	3.39	2.88	3.02
CaO	0.03	0.02	0.00
Na_2O	0.33	0.47	0.20
K_2O	10.15	10.02	10.62
Total	94.02	95.16	95.30
O = 11			
Si	3.48	3.39	3.36
Al	2.06	2.21	2.18
Mn	0.00	0.00	0.00
Mg	0.34	0.29	0.30
Ca	0.00	0.00	0.00
Na	0.04	0.06	0.03
K	0.87	0.85	0.91
Fe^{2+}	0.14	0.15	0.22
XMg	0.71	0.66	0.58

Abbreviations used: b.d., below detection; XMg = (Mg/Mg + Fe).
Samples are located on Figure 3a

more compact pseudomorph of quartz at the proximity of the quartz–coesite transition. This suggests minimum pressure conditions of 18 kbar (Wendt *et al.* 1993). These *P–T* conditions for the pressure peak are in agreement with minimal pressure estimates from previous studies (e.g. Simonov *et al.* 2008; Hegner *et al.* 2010) (Fig. 11).

The garnet rim crystallized during the retrograde stage. This rim is texturally in equilibrium with omphacite in the matrix. This omphacite has a jadeite content of 25 mol%, which suggests a minimum pressure of 9.5 and 11 kbar for 400 and 500°C, respectively (Holland 1983). Garnet–omphacite thermometry (Ravna 2000) indicates temperatures of 425–450°C for pressures of between 9.5 and 15 kbar. This temperature range is consistent with exhumation along a cold geothermal gradient at the transition between greenschist- and blueschist-facies conditions.

Pressure–temperature conditions of sediments hosting mafic eclogites

Mineralogy. Metasediments hosting mafic eclogite lenses contain high-pressure mineral relicts such as garnet and clinopyroxene (Fig. 8d). The fine-grained foliated matrix is made of calcite + phengite + quartz + chlorite. This matrix contains centimetre-scale nodules of clinopyroxene, with some occurrences of garnet and phengite. Garnet has calcite and quartz inclusions. The composition of garnet is homogeneous (Grs_{35-40} Alm_{55-60} Pyr_{5-10}). Clinopyroxene in the nodules (Fig. 5e) has omphacitic composition (Jd_{45}–Jd_{55}). The individual grains do not show any chemical zoning but the jadeite content varies from Jd_{45} to Jd_{55} from grain to grain. Phengite has a high Si content ranging from 3.36 to 3.42 p.f.u. (per formula unit.

P–T conditions. Garnet–omphacite thermometry (Ravna 2000) and garnet–omphacite–phengite geobarometry (Waters & Martin 1993; Waters 1996) indicate pressure conditions ranging from 19.8 to 21 kbar and temperatures from 450 to 480°C. Thermobarometry investigations were performed using phengite with the highest Si content. The *P–T* range results from the heterogeneities of the jadeite content in omphacite. *P–T* conditions suggest that metasediments underwent similar pressure conditions to those of mafic eclogites (20–21 kbar). However, the temperatures are slightly lower, ranging between 450 and 480°C for metasediments and 505–535°C for mafic eclogites. Following Lanari *et al.* (2013), we can assume an error

Table 5. *Trace element concentration (in ppm) measured in rutiles by LA-ICPMS (laser ablation inductively coupled plasma mass spectrometry) (sample KG-11-36, N 41° 02′ 0,43″, E 75° 42′ 17,18″, located in Fig. 3a)*

	Rutile					
	inc. Grt	Matrix	Matrix	Matrix	Matrix	Matrix
Li	6.11	0.04	–	0.14	0.20	0.09
Mg	5145	420	434	603	706	467
Al	6902	10	12	229	157	175
Si	8109	359	–	1165	540	–
Ca	1395.5	2.9	77.3	231.0	340.6	87.8
Sc	3.7	0.74	0.62	0.69	0.56	0.87
Ti	593 513	593 513	593 513	593 513	593 513	593 513
V	2087.2	1985.3	1984.5	1738.5	1778.8	1905.5
Cr	11.3	13.99	12.16	8.9	10.59	5.4
Mn	96.9	0.0	0.4	21.5	1.0	67.8
Fe	38 758	7410	6728	4914	5610	12 229
Rb	0.663	0.014	0.009	–	0.011	0.105
Sr	4.74	1.51	1.45	1.56	1.70	2.59
Yb	1.99	0.15	0.13	0.17	0.29	0.76
Zr	45.0	46.6	41.2	41.8	40.4	43.6
Nb	281	202	216	270	244	195
Mo	3.1	2.1	2.2	2.5	3.6	2.3
Ba	3.480	0.002	0.066	0.097	0.060	1.960
La	0.910	–	0.001	0.008	0.042	0.500
Ce	2.090	–	–	0.039	0.093	1.000
Pr	0.320	–	–	0.005	0.007	0.127
Nd	1.530	–	–	0.006	0.046	0.770
Sm	0.502	–	–	–	–	0.128
Eu	0.241	–	0.002	0.003	0.007	0.067
Gd	0.478	–	–	0.013	0.036	0.203
Tb	0.109	–	–			0.038
Dy	0.559	–	–	0.011	0.043	0.218
Ho	0.104	–	–	0.002	0.004	0.052
Er	0.316	–	–	0.004	–	0.175
Tm	0.028	–	–	–	–	0.024
Yb	0.209	–	–	0.015	–	0.202
Lu	0.035	–	–	–	–	0.016
Hf	3.4	3.1	2.8	3.0	3.2	3.2
Ta	24.2	13.7	15.0	21.1	14.6	10.1
^{206}Pb	8.900	0.012	0.021	0.200	0.195	1.660
^{208}Pb	8.260	0.005	0.003	0.193	0.208	1.660
Th	0.005	–	–	–	0.003	0.001
U	0.236	0.086	0.073	0.086	0.078	0.157
T (°C)	512.5	514.6	507.3	508.1	506.2	510.6

Temperature is calculated using the calibration of Ferry & Watson (2007).
Abbreviation used: inc. grt, inclusions in garnet.

linked to the microprobe uncertainty of ±20°C on temperature. The real uncertainty, when also considering the error on the thermodynamic data, is probably higher at ±50°C. In both cases, the temperature estimates obtained from metasediments and mafic eclogites are in good agreement.

Pressure–temperature conditions of continental gneisses

Mineralogy. As described above, the continental unit is made up of paragneisses with a paragenesis of albite + quartz + phengite + zoisite ± garnet ± chlorite. Quartz veins are often folded. Albite grains are millimetric–centimetric porphyroblasts with inclusions of phengite, garnet and zoisite (Fig. 10e, f). This texture indicates that they are pseudomorphs resulting from the destabilization of omphacite (Fig. 10e). Millimetric garnet grains are partially retrogressed into chlorite (Fig. 10f). Except for phengite, there is no remnant of a high-pressure assemblage in these samples. The secondary albite porphyroblasts suggest that the sample underwent high-pressure conditions before an

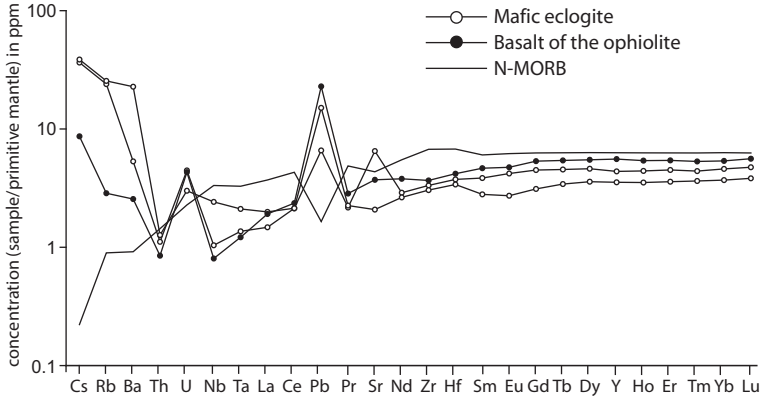

Fig. 9. Spider diagram of an unmetamorphosed basalt of the ophiolite and of mafic eclogites plotted along with typical N-MORB (Sun & McDonough 1989). Concentrations are normalized to primitive mantle concentrations (Sun & McDonough 1989).

intense and pervasive retrogression at lower P–T conditions. Furthermore, phengite has a high Si content (3.35–3.50 p.f.u. to the west of the range and 3.30–3.45 p.f.u. to the east), indicative of high-pressure conditions. These compositions are similar to those measured by Hegner *et al.* (2010) for a paragneiss sampled in the Kembel River.

Another feature suggesting that gneisses underwent high-pressure conditions is the shear zone at the upper boundary of the continental unit. This shear zone contains strongly deformed serpentinites with clino- and orthopyroxenes porphyroclasts. This argues for an upper-plate mantle lithosphere origin for these ultramafic rocks (Fig. 10g).

P–T conditions. In order to determine the P–T conditions of paragneisses, a pseudosection was calculated in the NCKFMASTiHO system with Theriak-Domino (De Capitani & Petrakakis 2010) using the thermodynamic database of Berman (1988) and subsequent updates (JUN92.bs) (Fig. 12). The effective bulk composition of the sample KG-12-74 (measured by ICP-MS) was used. The Si content in p.f.u. and XMg ($Mg/Mg + Fe$) in phengite isopleths were calculated. In addition, phengite + quartz + H_2O equilibria have been calculated for individual EPMA point analyses (Fig. 10h; Table 4) (Dubacq *et al.* 2010). This method can be used to estimate P–T conditions of crystallization of K-white mica in various environments (e.g. Lanari *et al.* 2012, 2014; Cantarero *et al.* 2014). Si content and XMg isopleths with phengite + quartz + H_2O equilibria intersect at $525 \pm 50^{\circ}C$ and 19 ± 2.5 kbar. In the different assemblages corresponding to these conditions, omphacite, white mica and garnet are predicted to be stable. Garnet and white mica are preserved during the subsequent retrogression. However, garnet is partially replaced by chlorite, and omphacite is not preserved during the retrogression stages. Omphacite reacts with quartz to form a secondary albite following the reaction jadeite + quartz → albite. The occurrence of clinozoisite in the gneisses indicates a retrograde stage near 420°C and 10 kbar in the stability field of clinozoisite and albite (Fig. 12). Consequently, this P–T path is similar to that of the mafic eclogite from the sedimentary mélange (see the earlier subsection on 'Pressure–temperature conditions of mafic eclogites').

Discussion

Synthesis of geological and seismic data: crustal-scale geometry of the STS

Metamorphic evolution of the STS (Kyrgyzstan and China). The similar metamorphic rocks found along the northern side of the STS in China and Kyrgyzstan (i.e. the kSTS and the cCTS + cSTS) are of prime importance for the reconstruction of crustal-scale sections and lateral correlations in the belt. The study of metamorphic rocks from Atbashi shows that oceanic (mafic eclogites) and continental (gneisses) units underwent relatively similar high-pressure conditions of about 20 kbar and 500°C. The preservation of the high-pressure mineral assemblage in the mafic eclogite without any retrogression in greenschist-facies conditions indicates either fast exhumation, at least faster than the metamorphic reactions kinetics, and/or an absence of circulating metamorphic fluids. The similarity between mafic eclogite and gneiss P–T paths also suggests a rapid exhumation for the continental unit. The strong retrogression in the

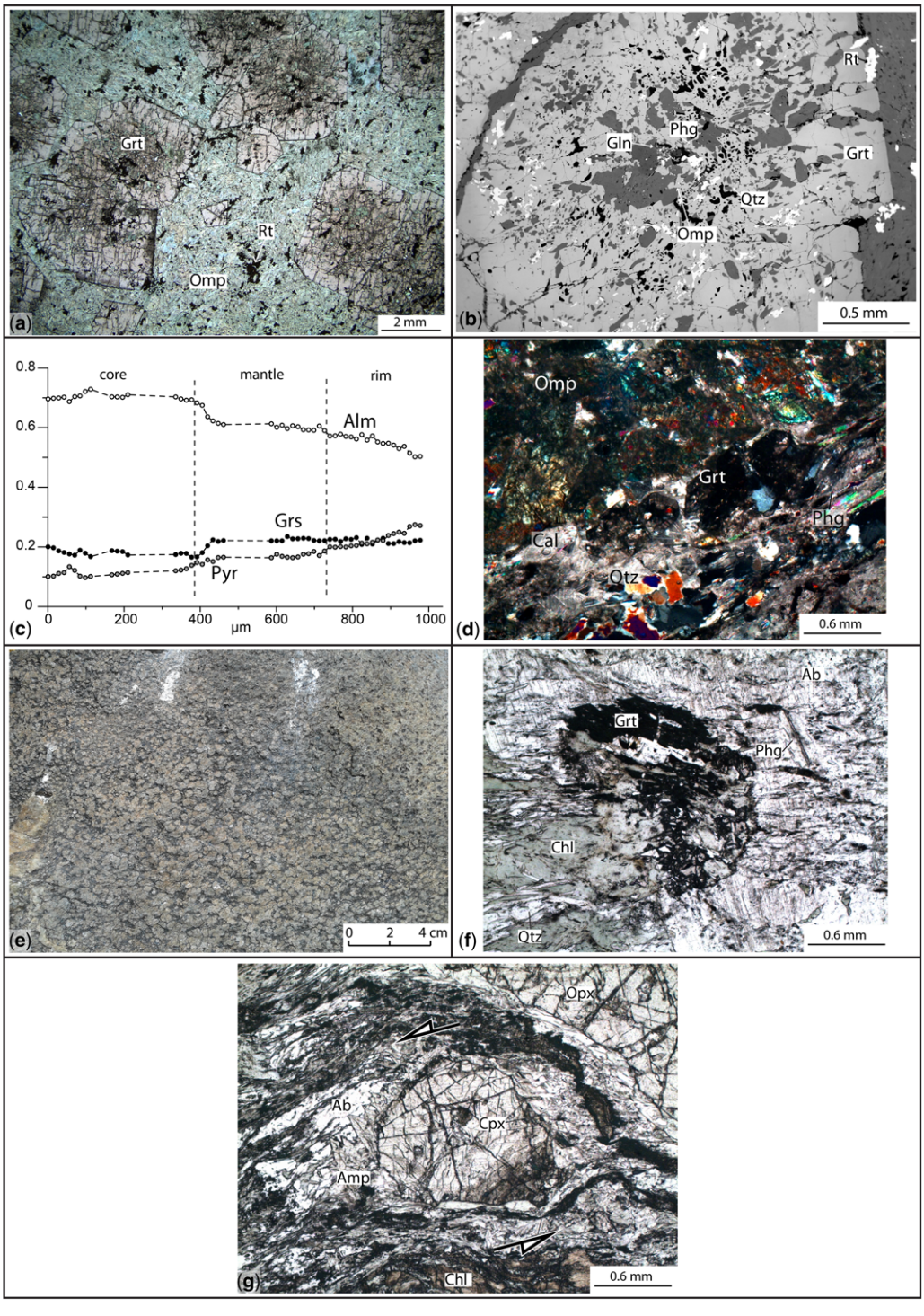

Fig. 10. Mineralogy and metamorphic conditions of Atbashi eclogites. Samples are located in Figure 3a. (**a**) Microphotograph in plane polarized light of mafic eclogite from the metasedimentary mélange of the high-pressure unit (sample KG-11-36) with garnet (Grt), omphacite (Omp) and rutile (Rt). (**b**) Backscattered electron image of a garnet

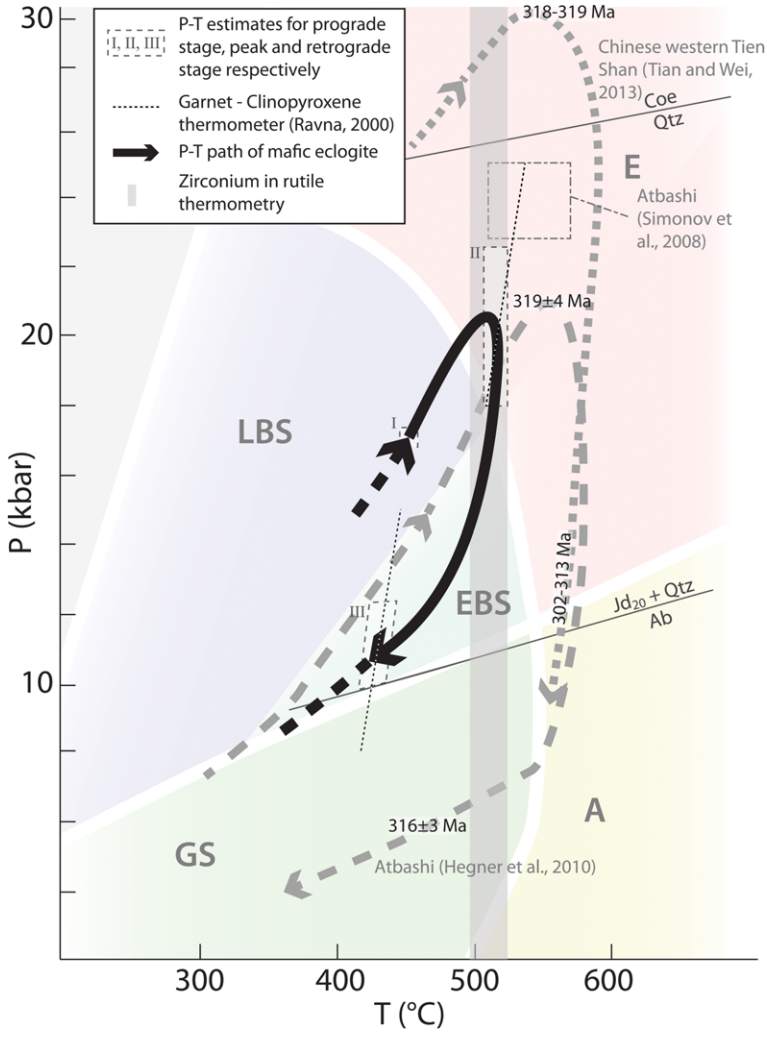

Fig. 11. Synthetic P–T path of mafic eclogites of Atbashi (black line) and comparison with results (P–T conditions and ages) of Simonov *et al.* (2008) and Hegner *et al.* (2010) for Atbashi and of Tian & Wei (2013) and Klemd *et al.* (2005) for the Chinese South Tien Shan (grey lines). The facies grid is after Evans (1990). Facies abbreviations: GS, greenschist; A, amphibolite; LBS, lawsonite blueschist; EBS, epidote blueschist; E, eclogite. The albite (Ab) = jadeite$_{20}$ (Jd) + quartz (Qtz) reaction is after Holland (1980). The quartz (Qtz)–coesite (Coe) reaction is after Bohlen & Boettcher (1982).

Fig. 10. (*Continued*) (sample KG-11-36) showing minerals that were included during garnet growth. Note that the garnet core bears phengite (Phg) + glaucophane (Gln, blueschist facies), while the garnet mantle bears omphacite and quartz (Qtz), and the external garnet (rim) has only omphacite inclusions. Rutile occurs in the mantle and rim of garnet. (**c**) Garnet compositional profile (sample KG-11-36) showing the three zones defined above on the basis of almandine (Alm), grossular (Grs) and pyrope (Py) content. (**d**) Microphotograph of metasedimentary eclogite (sample KG-12-58A) from the metasedimentary mélange of high-pressure unit showing in the upper part a nodule of omphacite + garnet, and in the lower part a matrix of phengite + calcite (Cal) + quartz (crossed polars). (**e**) Photograph of a gneiss from the continental high-pressure unit, showing secondary albite pseudomorphs (possibly after jadeite). (**f**) Microphotograph of gneiss from the high-pressure continental unit (plane polarized light), showing a garnet included in a secondary albite. The garnet is partly replaced by chlorite. (**g**) Microphotograph of a strongly deformed serpentinite in the shear zone between the high-pressure continental unit and the greenschist facies upper unit showing sheared clinopyroxene (plane polarized light).

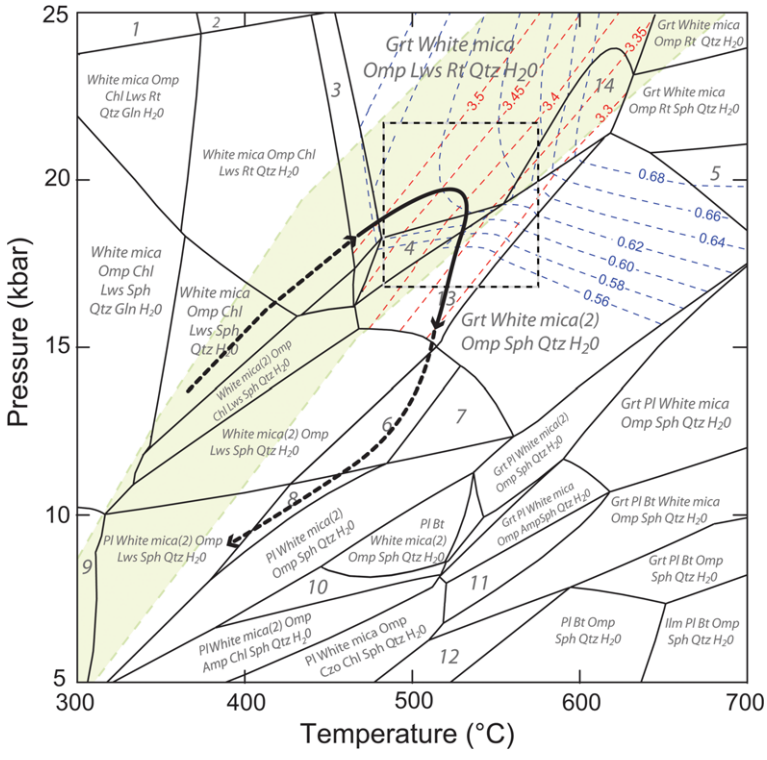

Fig. 12. Pressure–temperature (P–T) path of the high-pressure continental unit gneiss. The sample is located on Figure 3. The pseudosection is computed from the effective bulk composition of the KG-12-74 sample (mol): Si(1.12) Al(0.180) Fe(0.06) Mg(0.05) Ca(0.11) Na(0.06) Ti(0.01) K(0.02) H(0.53) O(?), in the system NKCFMASTiHO using Theriak-Domino software (De Capitani & Petrakakis 2010) with the thermodynamic database of Berman (1988). Si-in-phengite (p.f.u.) and X_{Mg} (Mg/(Fe + Mg)) of phengite isopleths are added as red dashed lines and blue dashed lines, respectively. The field of phengite + quartz + H_2O equilibria is calculated with the method of Dubacq *et al.* (2010) and shown in green. The black dashed box represents the range of pressure–temperature conditions obtained for the metamorphic peak of the gneisses from the continental high-pressure unit. Abbreviations used: Grt, garnet; Omp, omphacite; Qtz, quartz; Coe, coesite; Pl, plagioclase; Gln, glaucophane; Amp, amphibole; Chl, chlorite; Lws, lawsonite; Rt, rutile; Sph, titanite. 1: white mica Lws Rt Coe Gln H_2O; 2: white mica Omp Chl Lws Rt Coe H_2O; 3: Grt white mica Omp Chl Lws Rt Qtz Gln H_2O; 4: Grt white mica(2) Omp Lws Rt Qtz Gln H_2O; 5: Grt white mica Omp Sph Qtz H_2O; 6: white mica(2) Omp Czo Sph Qtz H_2O; 7: white mica(2) Omp Sph Qtz H_2O; 8: Fd white mica(2) Omp Czo Sph Qtz H_2O; 9: Fd white mica(2) Omp Chl Lws Sph; 10: Fd white mica(2) Omp Chl Sph Qtz H_2O; 11: Grt Fd Bt white mica Omp AmpSph Qtz H_2O; 12 : Fd Bt white mica Omp Sph Qtz H_2O; 13: Grt white mica(2) Omp Lws Sph Qtz H_2O; 14: Grt white mica Omp Lws Rt Sph Qtz H_2O.

gneisses is ascribed to a high fluid/rock ratio due to the sedimentary origin of the gneisses. This rapid exhumation is also represented by within-error Sm–Nd and $^{40}Ar/^{39}Ar$ ages of 319–316 Ma on mafic eclogites (Hegner *et al.* 2010). These ages represent cooling from the peak temperature, as the closure temperature of the Sm–Nd system is around 600°C (Mezger *et al.* 1992), down to about 380°C (Robbins 1972; Hames & Bowring 1994). This metamorphic evolution is very similar to that obtained in the western Chinese STS (Tian & Wei 2013). Although pressure and temperature estimates (up to 30 kbar and 550°C) are slightly higher in China (Fig. 11), the U–Pb and Ar/Ar ages are similar (*c.* 319–310 Ma) (Klemd *et al.* 2005; Su *et al.* 2010; Li *et al.* 2011). The minimum age for eclogite exhumation in Atbashi is provided by the occurrence of eclogite pebbles in conglomerates dated at approximately 303–295 Ma (Baslakunov *et al.* 2007). This implies an average exhumation rate >3 mm a^{-1} from peak high-pressure conditions to the surface. New observations of a large continental thrust sheet, composed of high-pressure gneisses and subducted to a similar depth as the oceanic crust in Atbashi, is documented by the presence of mafic eclogites. This indicates that continental subduction occurred, similar to the Dora-Maira Massif in the Western Alps (Chopin 1984). A

similar high-pressure unit is described in an identical structural position in China. There, coesite has been described in continental schists hosting some mafic eclogites (Yang *et al.* 2011; Lü *et al.* 2012). These data show that the high-pressure units of the STS from Kyrgyzstan and China, although separated by 500 km, represent the same units with a similar geodynamic history and similar structural position. It is a very strong geological argument for the lateral cylindricity of the belt, and for the construction of crustal-scale cross-sections along the STS, as these high-pressure units must be present at depths all along the northern margin of the Tarim Basin.

Crustal-scale cross-sections of the STS. Based on these data and new geological mapping, we propose a reinterpretation of the MANAS seismic profile (Makarov *et al.* 2010) along the Atbashi Range (Fig. 13a). In the original interpretation, some south-verging reflectors are neglected in the northern half of the profile (see fig. 10 in Makarov *et al.* 2010). In this new cross-section, we follow the original interpretation made by these authors

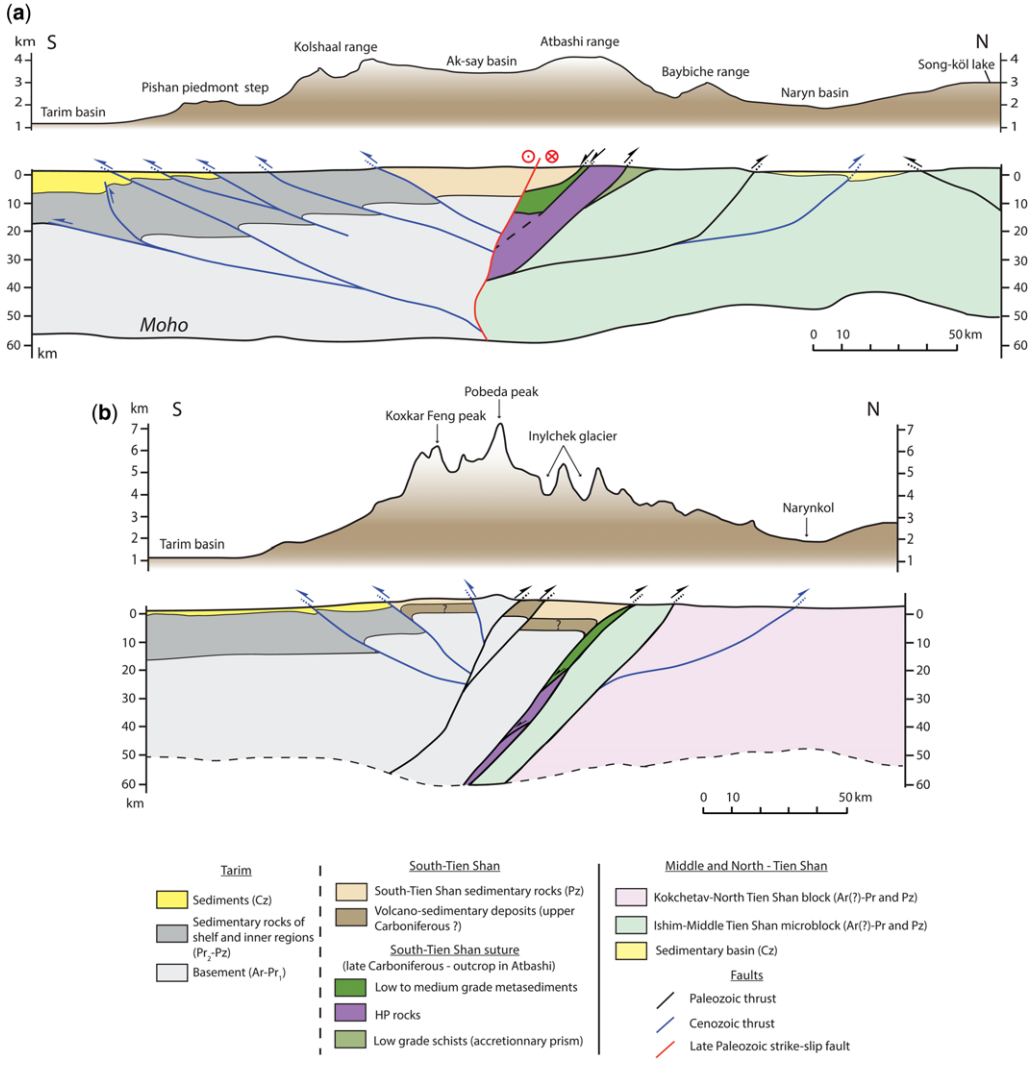

Fig. 13. (**a**) Crustal-scale cross-section of western South Tien Shan after reinterpretation of the crustal-scale Manas seismic profile (Makarov *et al.* 2010). (**b**) Crustal-scale cross-sections of eastern Kyrgyz South Tien Shan crossing the highest part of the belt, the Pobeda Khan-Tengri Massif. Abbreviations used: Ar, Archean; Pz, Palaeozoic; Cz, Cenozoic. Cross-sections are located in Figure 2b.

for the southern part of the kSTS: that is, where the Tarim block is cross-cut by several active south-verging thrusts uplifting the Upper Protezoic–Palaeozoic sedimentary series of the STS (Fig. 2). Based on surface geological data presented in this paper and the south-dipping reflectors, we propose a north-vergent thrust stack to the north of the STS. These thrusts were reactivated during Recent tectonicism, as shown by uplifted alluvial terraces along the northern side of Atbashi Range (Fig. 3). An overall positive flower-type structure is observed in the STS. The oppositely verging thrusts are separated by a subvertical strike-slip fault with possible left-lateral motion of Permian age (Biske 1995; Alexeiev *et al.* 2007) (Fig. 5i).

A second crustal-scale cross-section is drawn across the Pobeda Massif, between the Atbashi Range and the Chinese STS (Fig. 13b). There, the mountain belt is higher and narrower. We interpret this major difference as the result of a more focused (i.e. less distributed) deformation. On the south side, three thrusts are observed on satellite images (Fig. 2), while the highest summit of the range (the Pobeda Peak, 7400 m) appears to be composed of Tarim Basement exposed in a narrow positive flower-structure. On the northern side, a similar top-to-the-north thrust sequence is suggested by geological mapping. However, the high-pressure units are not exposed in this part of the belt. We propose that this absence results from a more significant Cenozoic offset along the north-verging faults, which has hidden these units. These units reappear further to the east in China. The narrow positive flower-structure could be explained by a strike-slip component, which has not, however, been found in the field.

The timing of deformations in the STS. The following history is proposed for the different faults:

- The north-verging thrust sequence is at least partly Carboniferous in age, as inferred from the pressure gap between high-pressure units and unmetamorphosed ophiolites. Furthermore, Upper Carboniferous–Lower Permian conglomerates lie discordantly on this top-to-the-north thrust stack. This top-to-the-north motion is ascribed to the Tarim–Middle Tien Shan accretion or collision in Kyrgyzstan, and to Central Tien Shan/Yili–North Tien Shan accretion in China (e.g. Charvet *et al.* 2007). At a regional scale, the story is simplified to the collision/accretion of the Tarim block with the Kazakh continent. This episode occurred at approximately 320–310 Ma, and is thus the last accretionary event of the CAOB.
- The vertical strike-slip fault separating the two opposite vergences domains is thought to have a main Late Palaeozoic (Permian) activity (Alexeiev *et al.* 2007). The left-lateral sense of shear would be consistent with the right-lateral sense of shear observed along the Talas–Fergana Fault (e.g. Rolland *et al.* 2013).
- The south-vergent thrusts are thought to be mainly Cenozoic in age. They may have been initiated during the Late/post-collisional Carboniferous history (Biske & Seltmann 2010; Charvet *et al.* 2011; Lin *et al.* 2013). However, there is no significant offset on these faults, as argued by the absence of exhumed deep-crustal levels. Thus, the major offset on these faults is Cenozoic, as the seismic profile shows significant thrusting of Palaeozoic formations on the Tarim Basin (Makarov *et al.* 2010).

STS Ocean subduction polarity?

One of the major issues considering the tectonic evolution of the STS is the polarity of the Central Tien Shan Ocean subduction (or palaeo-Tien Shan Ocean). Diverse interpretations have been proposed:

- Several authors propose that there was north-dipping subduction below the Middle Tien Shan in Kyrgyzstan or below the Yili block in China (e.g. Windley *et al.* 1990; Allen *et al.* 1992; Biske 1996; Gao & Klemd 2003; Xiao 2004; Zhang *et al.* 2007; Makarov *et al.* 2010; Hegner *et al.* 2010; Han *et al.* 2011). This model is based on: (i) some top-to-the-south thrusts observed on the southern flank of the kSTS (e.g. Biske & Seltmann 2010); (ii) asymmetric folds exhibiting top-to-the-south sense of shear (Porshnyakov 1983; Alexeiev *et al.* 2007); and (iii) the absence of a volcanic arc in the kSTS (e.g. Tursungaziev & Petrov 2008). However, this last argument is rather weak because, in the Chinese Tien Shan, there is an Ordovician–early Devonian volcanic arc to the south of the cCTS suture (T. N. Yang *et al.* 2006; Li *et al.* 2008).
- Alternatively, other authors propose that there was south-dipping subduction (e.g. Charvet *et al.* 2007, 2011; Wang *et al.* 2008; Lin *et al.* 2009; Ma *et al.* 2014; Zhao *et al.* 2015). This latter interpretation is mainly based on the overall south-dipping structure and the Ordovician–early Devonian volcanic arc to the south of the cCTS suture (T. N. Yang *et al.* 2006; Li *et al.* 2008). In this model, the Central Tien Shan Ocean was subducted southwards beneath the cCTS from the Ordovician to the Late Devonian–Early Carboniferous. During the Ordovician, the cCTS was still part of the northern edge of the Tarim block. In the Late Silurian, this southward subduction leads to the opening

of a back-arc basin (i.e. the South Tien Shan Ocean) separating the cCTS from the Tarim block (e.g. Wang *et al.* 2011). This back-arc basin was subducted southwards beneath the Tarim block from Devonian to Early Carboniferous times, generating arc volcanism on the northern edge of the Tarim block (Jiang *et al.* 2001; Ma 2002; Lin *et al.* 2013; Zhao *et al.* 2015).

On the basis of field investigations along the entire northern side of the Kyrgyz STS, we describe a coherent and continuous structure characterized by top-to-the-north thrusts. These thrusts are locally associated with top-to-the-south detachments where the high-pressure units are exhumed (in the Atbashi section) (Figs 2 & 3). The formation of these structures is best explained by south-dipping subduction. If the subduction was top-to-the-north, the structure would have to be homogeneously tilted 90° along strike from Atbashi to China, which is unlikely. The south-vergent thrusts located on the southern flank of the STS and on the northern edge of Tarim are mostly Cenozoic, which explains the double vergence of the mountain range. In Kyrgyzstan, unlike in China, there is no arc associated with this subduction, and no evidence for long-lasting subduction (ages of high-pressure metamorphism range between *c.* 320 and 310 Ma). Thus, it seems that the size of the oceanic basin was smaller to the west in Kyrgyzstan compared to that in China. Another interpretation, which may be complementary, is that the corresponding arc series are hidden below the Carboniferous sedimentary series and remain unexposed.

This style of orogeny is similar to that of the Western Alps in the Oligocene. There, a similar succession of metamorphic units and the absence of a magmatic arc are observed, which could be due to the subduction of a narrow oceanic basin (e.g. Handy *et al.* 2010). A similar structure and metamorphic evolution as that of the STS is well reproduced by a thermomechanical model (Vogt & Gerya 2014), which has been slightly modified to reflect the regional geology and is briefly described below.

Geodynamic model for the Carboniferous tectonics of the STS

Vogt & Gerya (2014) modelled the subduction of a plateau or a small continental block separated from a major continental boundary by a small, approximately 500 km-wide oceanic domain. In our regional setting, the small continental block should be connected to the Middle Tien Shan by a highly thinned or rifted continental margin. According to the numerical model of Vogt & Gerya (2014), subduction of the small continental block leads to exhumation of high-pressure–ultra-high-pressure continental rocks and partial melting of the internal part of the mountain belt (Fig. 14). This model broadly matches the geodynamic setting of the STS during Carboniferous times.

During the first stage (Fig. 14a, b), south-dipping oceanic subduction beneath the Tarim block initiated before about 327 Ma, the oldest age of the high-pressure metamorphism (Simonov *et al.* 2008). An accretionary prism containing low-grade rocks and ophiolites is formed at the same time. Slab-pull on the small continental block driven by the eclogitized oceanic crust leads to its subduction to mantle depth. Rapidly, the negative buoyancy of the subducting continent leads to slab breakoff, which induces asthenospheric upwelling, documented by granitic magmatism (Song *et al.* 2013). The lack of arc magmatism and geochronological data for the prograde history of high-pressure rocks does not allow the age of subduction onset to be constrained, thus it remains difficult to pinpoint this age. However, Stern *et al.* (2012) suggested that at least 7 Ma are necessary for the complete transition from initial seafloor spreading to ongoing subduction. Considering that the oldest age for the high-pressure metamorphism is 327 Ma, it suggests a minimal age of 334 Ma for the onset of subduction. Further, the dated exhumed high-pressure rocks are not necessarily the oldest and, consequently, this initiation age could be older.

Following slab breakoff, the eclogitized continental crust is uplifted and stacked at the base of the continental crust of the upper plate (Fig. 14c). In the case of the Tien Shan, this uplift could also be induced by the underthrusting of the thicker Middle Tien Shan units, and thus correspond to a transition from a subduction to a 'true' collision. In the external part, the eclogites are exhumed along a cold geothermal gradient and overthrust the low-grade accretionary prism. During this exhumation, deep parts of the accretionary prism and serpentinized mantle may be dragged up with the high-pressure continental unit (Guillot *et al.* 2009), as observed in Atbashi. Eclogitized sedimentary mélange is found on the north side of the high-pressure continental unit, while, on the south side, serpentinites limit a major detachment. The internal part is heated by the inflow of uprising asthenosphere. Consequently, the high-pressure rocks exhibit a hot retrograde path in the granulite facies, documenting partial melting in the lower–intermediate crust. Finally, crust–mantle magmatic mixing results in uprising calc-alkaline granitic intrusions in the upper crust (Fig. 14d). In the model, only 11 myr are necessary from the peak metamorphism to the exhumation of high-pressure rocks. However the geological and

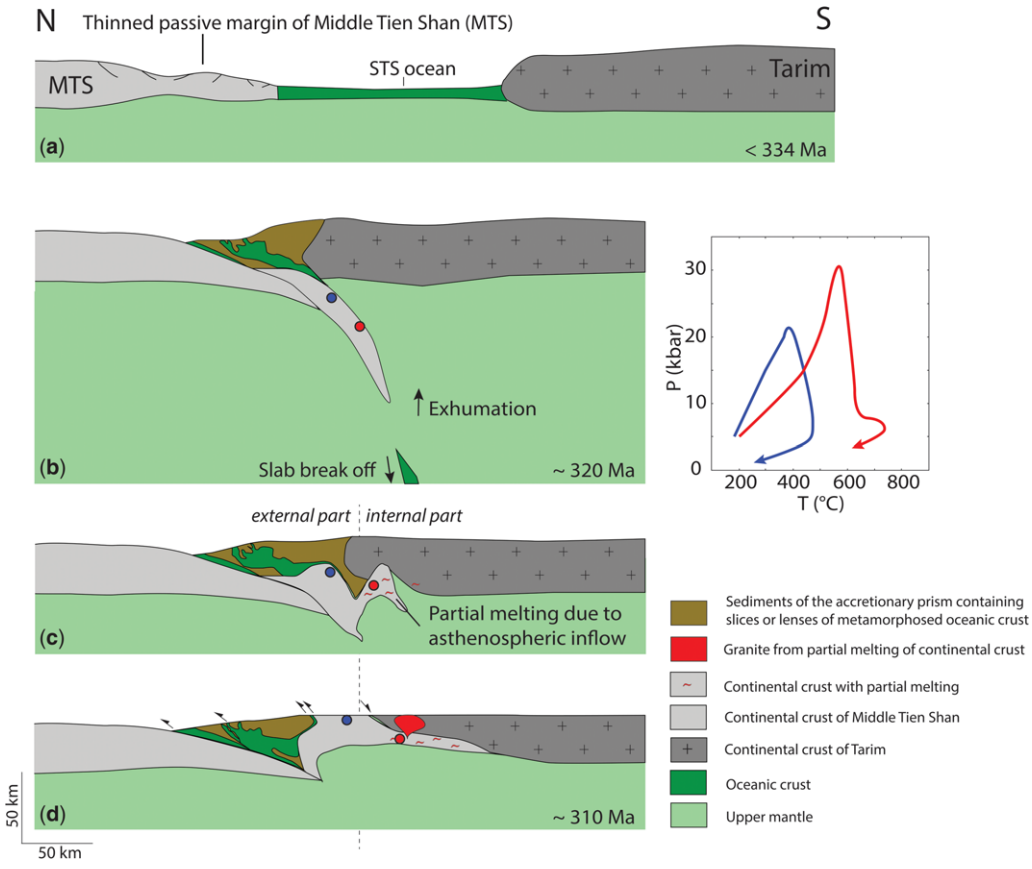

Fig. 14. Geodynamic evolution of the South Tien Shan in Carboniferous times, based on the model of Vogt & Gerya (2014). The blue and red paths in the P–T grid represent characteristic paths for rocks from the external (frontal) (the blue point in the illustration represent the Atbashi Range high-pressure rocks) and from the internal part (the red point in the illustration) of the upper plate, respectively. See comments in the text.

geochronological constraints for the Atbashi eclogites suggest that the exhumation from the pressure peak to the surface lasted around 20 myr, taking into account the dates of 319 Ma for the high-pressure metamorphism (Hegner *et al.* 2010) and 295–303 Ma for the exhumation at the surface featured by conglomerates unconformably resting on the high-pressure rocks (Baslakunov *et al.* 2007).

In summary, the geological constraints obtained for the STS are broadly consistent with the model of Vogt & Gerya (2014). (i) The presence and the particular succession of geological units from north to south: an accretionary prism, an unmetamorphosed relict of oceanic crust (ophiolite), a first high-pressure unit corresponding to the base of the accretionary prism (the eclogitized sedimentary mélange), and a second high-pressure unit composed of continental eclogites, serpentinites and calc-alkaline granites intruding the upper crust of the Tarim block. (ii) The overall south-dipping structure. (iii) Kinematics with both top-to-the-north thrusting and top-to-the-south detachment on the rims of the extruded high-pressure continental unit. (iv) Pressure–temperature–time (P–T–t) paths of high-pressure rocks, which remain cold in the external units. Following this model, the Pobeda granulites exhumed by the Cenozoic Pobeda Thrust might represent either the subducted crust that underwent partial melting in the internal part in Carboniferous or older basement corresponding to the Tarim block. Dating of the Pobeda granulites may help to distinguish between these two possibilities. Collision, indicated by this exhumation, would then have been the final event of the Central Asian orogenic belt's accretionary history.

However, the model is not consistent with the geochronological constraints which suggest that the time elapsed between the high-pressure

metamorphism and the exhumation of high-pressure rocks is about twice as long as that in the model (20 Ma for the STS, 11 Ma in the model). This discrepancy between observations and the numerical model could be explained by differences in the initial setting: for example, in the convergence velocity or in the size of the subducted block. Moreover, the final exhumation age is a minimum age, provided by the emplacement of the conglomerates. Further thermochronological data are necessary to constrain the complete exhumation history and, possibly, highlight different exhumation stages. Thus, this numerical model gives a general idea of mechanisms involved in the formation of the STS but further data and modelling will be necessary.

Conclusions

New field and petrological investigations along the STS belt in Kyrgyzstan, together with regional-scale geological mapping and crustal-scale cross-sections, allow us to correlate the main faults and units from Kyrgyzstan to China at the scale of the STS belt. The overall structure corresponds to a doubly-vergent mountain belt, with major top-to-the-north thrusts on the northern side and top-to-the-south thrusts on the southern side of the belt, separated by a subvertical contact. Towards the inner part of the STS belt in the Pobeda Massif, a push-up structure is exposed, cored by granulite-facies basement rocks thrust towards the north onto low-grade Devonian–Carboniferous schists. This basement may belong to the Tarim block or to crust granulitized during Carboniferous subduction.

On the northern side of the STS, the low-grade Devonian–Carboniferous schists exhibit a tectonic contact with high-pressure metamorphics in the Atbashi (Kyrgyzstan) and Kebuerte–Kekesu (China) areas. The two areas display identical structures as well as metamorphic histories that are consistent with a rapid metamorphic cycle during the accretion of the Tarim block with the CAOB at approximately 320–310 Ma. In Atbashi, a north-verging nappe stack is found that we ascribe to different parts of a subduction prism emplaced on top of the presumed Middle Tien Shan gneissic basement. This subduction prism is made up of unmetamorphosed to eclogite-facies ophiolites. The pressure–temperature (P–T) path of mafic eclogites is constrained by peak conditions of 510 ± 25°C using Zr-in-rutile thermometry at $P > 18$ kbar, and retrogression along a cold geothermal gradient at 425–450°C and 9.5–15 kbar. P–T estimates on metasediments hosting mafic eclogite boudins provide similar estimates (450–480°C, 19.8–21 kbar), in agreement with the presence of a sedimentary subduction channel extending down to mantle depths. These high-pressure oceanic units are overthrust by a large unit of continental gneiss, which was also subducted to mantle depths in similar conditions (505 ± 50°C and 19 ± 2.5 kbar), with a similar exhumation path (i.e. in cold conditions). The contact of this high-pressure continental unit with the southern STS/probable margin of Tarim is a south-dipping detachment showing an extensional top-to-the-south sense of shear. The contact is emphasized by stretched peridotites attributed to the upper-plate lithosphere.

The structural and metamorphic data are consistent with south-dipping subduction and subsequent subduction of an ultra-stretched continental margin belonging to the Middle Tien Shan. This evolution is broadly consistent with a published numerical model of Vogt & Gerya (2014). The time span for this collision–accretion orogeny is at least 27 myr between onset of subduction and final exhumation.

Subsequent reactivation during Permian–Mesozoic times occurred mainly in a strike-slip regime, featuring left-lateral motion localized in the centre of the STS. Later, during the Cenozoic, a flower structure developed through the reactivation of former top-to-the-north Carboniferous thrusts to the north of the STS and activation of the top-to-the-south thrusts in a fold-and-thrust belt propagating over the Tarim block, south of the STS.

This work was supported by the DARIUS Programme and the ANR DSP-Tibet. The authors warmly thank the help and support of M. F. Brunet and E. Barrier for the coordination of this project and the organization of related workshops. D. V. Alexeiev is warmly thanked for his help in the field, discussions and comments on a preliminary version of the manuscript. E. Sobel, J. Charvet, R. Oberhänsli and an anonymous reviewer are thanked for their constructive comments that improved the manuscript. We also appreciate the help of A. K. Rybin, Director of the Research Station of the Russian Academy of Sciences in Bishkek, for help with logistics and organizational support.

References

Abdrakhmatov, K., Weldon, R., Thompson, S. C., Burbank, D. W., Rubin, C., Miller, M. & Molnar, P. 2001. Onset, style and current rate of shortening in the central Tien Shan, Kyrgyz Republic. *Russian Geology and Geophysics*, **42**, 1585–1609.

Abdrakhmatov, K. Y., Aldazhanov, S. A. *et al*. 1996. Relatively recent construction of the Tien Shan inferred from GPS measurements of present-day crustal deformation rates. *Nature*, **384**, 450–453.

Alekseev, D. V., Aristov, V. A. & Degtyarev, K. E. 2007. The age and tectonic setting of volcanic and cherty sequences in the ophiolite complex of the Atbashe Ridge (Southern Tien Shan). *Doklady Earth Sciences*, **413**, 380–383.

ALLEN, M. B., WINDLEY, B. F. & CHI, Z. 1992. Paleozoic collisional tectonics and magmatism of the Chinese Tien-Shan, Central-Asia. *Tectonophysics*, **220**, 89–115.

ALLEN, M. B., ALSOP, G. I. & ZHEMCHUZHNIKOV, V. G. 2001. Dome and basin refolding and transpressive inversion along the Karatau Fault System, southern Kazakstan. *Journal of the Geological Society, London*, **158**, 83–95, http://doi.org/10.1144/jgs.158.1.83

BAKIROV, A. B. 1978. *Tectonic Position of Metamorphic Complexes in Tianshan*. Ilim, Frunze (in Russian).

BAKIROV, A. B. & KOTOV, V. V. 1988. Eclogite-bearing metamorphic complexes as indicator of the ancient continent collision zone. *In*: *Precambrian and Lower Paleozoic of Tianshan*. Ilim, Frunze, 4–25 (in Russian).

BANDE, A., SOBEL, E. R., MIKOLAICHUK, A. & TORRES, A. V. In press. Talas–Fergana Fault Cenozoic timing of deformation and its relation to Pamir indentation. *In*: BRUNET, M.-F., MCCANN, T. & SOBEL, E. R. (eds) *Geological Evolution of Central Asian Basins and the Western Tien Shan Range*. Geological Society, London, Special Publications, **427**, http://doi.org/10.1144/SP427.1

BASLAKUNOV, J., TAKASU, A., TAGIRI, M., BAKIROV, A. & SAKIEV, K. 2007. Two modes of occurrence of eclogites from the Atbashy Range, southern Tien-Shan, Kyrgyzstan. *In*: *Proceedings of the American Geophysical Union Fall Meeting*. American Geophysical Union, Washington, DC, Abstract V41C0730B.

BERMAN, R. G. 1988. Internally-consistent thermodynamic data for minerals in the system Na_2O–K_2O–CaO–MgO–FeO–Fe_2O_3–Al_2O_3–SiO_2–TiO_2–H_2O–CO_2. *Journal of Petrology*, **29**, 445–522.

BISKE, Y. S. 1995. Late Paleozoic collision of Kirghiz-Kazahkstan and Tarim paleocontinents. *Geotectonics*, **1**, 31–39.

BISKE, Y. S. 1996. *Paleozoic Structure and History of South Tian-Shan*. Sankt-Pete, St-Petersburg (in Russian).

BISKE, Y. S. & SELTMANN, R. 2010. Paleozoic Tian-Shan as a transitional region between the Rheic and Urals-Turkestan oceans. *Gondwana Research*, **17**, 602–613.

BISKE, Y. S., ZUBTOV, Y. S. & PORSHNYAKOV, G. S. 1985. *Hercynides of the Atbashi-Kokshaal Region on the Southern Tian-Shan*. Leningrad State University, Leningrad (in Russian).

BISKE, Y. S., KONOPELKO, D. L. & SELTMANN, R. 2013. Geodynamics of late Paleozoic magmatism in the Tien Shan and its framework. *Geotectonics*, **47**, 291–309.

BOHLEN, S. R. & BOETTCHER, A. L. 1982. The quartz ⇆ coesite transformation: a precise determination and the effects of other components. *Journal of Geophysical Research*, **87**, 7073.

BOSCH, D., GARRIDO, C. J., BRUGUIER, O., DHUIME, B., BODINIER, J. L., PADRÒN-NAVARTA, J. A. & GALLAND, B. 2011. Building an island-arc crustal section: time constraints from a LA-ICP-MS zircon study. *Earth and Planetary Science Letters*, **309**, 268–279.

BRUGUIER, O., HAMMOR, D., BOSCH, D. & CABY, R. 2009. Miocene incorporation of peridotite into the Hercynian basement of the Maghrebides (Edough massif, NE Algeria): implications for the geodynamic evolution of the Western Mediterranean. *Chemical Geology*, **261**, 171–183.

BULLEN, M. E., BURBANK, D. W., GARVER, J. I. & ABDRAKHMATOV, K. Y. 2001. Late Cenozoic tectonic evolution of the northwestern Tien Shan: new age estimates for the initiation of mountain building. *Geological Society of America Bulletin*, **113**, 1544–1559.

BULLEN, M. E., BURBANK, D. W. & GARVER, J. I. 2003. Building the Northern Tien Shan: integrated thermal, structural, and topographic constraints. *Journal of Geology*, **111**, 149–165.

BURTMAN, B. S. 2006. The Tien Shan early Paleozoic tectonics and geodynamics. *Russian Journal of Earth Sciences*, **8**, 1–23.

CANTARERO, I., LANARI, P., VIDAL, O., ALÍAS, G., TRAVÉ, A. & BAQUÉS, V. 2014. Long-term fluid circulation in extensional faults in the central Catalan Coastal Ranges: P–T constraints from neoformed chlorite and K-white mica. *International Journal of Earth Sciences*, **103**, 165–188.

CARROLL, A. R., GRAHAM, S. A., HENDRIX, M. S., YING, D. & ZHOU, D. 1995. Late Paleozoic tectonic amalgamation of northwestern China–sedimentary record of the northern Tarim, northwestern Turpan, and southern Junggar basins. *Geological Society of America Bulletin*, **107**, 571–594.

CHANG, J., QIU, N. & LI, J. 2012. Tectono-thermal evolution of the northwestern edge of the Tarim Basin in China: constraints from apatite (U–Th)/He thermochronology. *Journal of Asian Earth Sciences*, **61**, 187–198.

CHARREAU, J., GILDER, S. *ET AL.* 2006. Magnetostratigraphy of the Yaha section, Tarim Basin (China): 11 Ma acceleration in erosion and uplift of the Tian Shan Mountains. *Geology*, **34**, 181.

CHARVET, J., LAURENT-CHARVET, S., SHU, L. & MA, R. 2001. Paleozoic continental accretions in Central Asia around Junggar Block: new structural and geochronological data. *Gondwana Research*, **4**, 590–592.

CHARVET, J., SHU, L. L. S. & LAURENT-CHARVET, S. 2007. Paleozoic structural and geodynamic evolution of eastern Tianshan (NW China): welding of the Tarim and Junggar plates. *Episodes*, **30**, 162–172.

CHARVET, J., SHU, L. *ET AL.* 2011. Palaeozoic tectonic evolution of the Tianshan belt, NW China. *Science China Earth Sciences*, **54**, 166–184.

CHEN, C., LU, H., JIA, D., CAI, D. & WU, S. 1999. Closing history of the southern Tianshan oceanic basin, western China: an oblique collisional orogeny. *Tectonophysics*, **302**, 23–40.

CHEN, H. L., YANG, S. F. *ET AL.* 2009. 2009. Spatial and temporal characteristics of Permian large igneous province in Tarim Basin (in Chinese with English abstract). *Xinjiang Petroleum Geology*, **30**, 179–182.

CHOPIN, C. 1984. Coesite and pure pyrope in high-grade blueschists of the Western Alps: a first record and some consequences. *Contributions to Mineralogy and Petrology*, **86**, 107–118.

DE CAPITANI, C. & PETRAKAKIS, K. 2010. The computation of equilibrium assemblage diagrams with Theriak/Domino software. *American Mineralogist*, **95**, 1006–1016.

De Grave, J., Buslov, M. M. & Van den haute, P. 2007. Distant effects of India–Eurasia convergence and Mesozoic intracontinental deformation in Central Asia: constraints from apatite fission-track thermochronology. *Journal of Asian Earth Sciences*, **29**, 188–204.

De Grave, J., Glorie, S. *et al.* 2011. The thermo-tectonic history of the Song-Kul plateau, Kyrgyz Tien Shan: constraints by apatite and titanite thermochronometry and zircon U/Pb dating. *Gondwana Research*, **20**, 745–763.

De Grave, J., Glorie, S. *et al.* 2012. Late Palaeozoic and Meso-Cenozoic tectonic evolution of the southern Kyrgyz Tien Shan: constraints from multi-method thermochronology in the Trans-Alai, Turkestan-Alai segment and the southeastern Ferghana Basin. *Journal of Asian Earth Sciences*, **44**, 149–168.

De Grave, J., Glorie, S., Buslov, M. M., Stockli, D. F., McWilliams, M. O., Batalev, V. Y. & Van den haute, P. 2013. Thermo-tectonic history of the Issyk-Kul basement (Kyrgyz Northern Tien Shan, Central Asia). *Gondwana Research*, **23**, 998–1020.

de Jong, K., Wang, B. B. *et al.* 2008. New $^{40}Ar/^{39}Ar$ age constraints on the late Palaeozoic tectonic evolution of the western Tianshan (Xinjiang, northwestern China), with emphasis on Permian fluid ingress. *International Journal of Earth Sciences*, **98**, 1239–1258.

Dubacq, B., Vidal, O. & De Andrade, V. 2010. Dehydration of dioctahedral aluminous phyllosilicates: thermodynamic modelling and implications for thermobarometric estimates. *Contributions to Mineralogy and Petrology*, **159**, 159–174.

Dumitru, T. A., Zhou, D., Chang, E. Z., Graham, S. A., Hendrix, M. S., Sobel, E. R. & Carroll, A. R. 2001. Uplift, exhumation, and deformation in the Chinese Tian Shan. *In*: Hendrix, M. S. & Davis, G. A. (eds) *Paleozoic and Mesozoic Tectonic Evolution of Central and Eastern Asia–From Continental Assembly to Intracontinental Deformation*. Geological Society of America, Memoirs, **194**, 71–99.

Enkin, R., Yang, Z., Chen, Y. & Courtillot, V. 1992. Paleomagnetic constraints on the geodynamic history of the major blocks of China from the Permian to the present. *Journal of Geophysical Research*, **97**, 13 953–13 989.

Evans, B. 1990. Phase relations of epidote- blueschists. *Lithos*, **25**, 3–23.

Ferry, J. M. & Watson, E. B. 2007. New thermodynamic models and revised calibrations for the Ti-in-zircon and Zr-in-rutile thermometers. *Contributions to Mineralogy and Petrology*, **154**, 429–437.

Fortuna, A. B., Kerimbekov, C. K. I. K. S. & Mikolaichuk, A. V. 1994. Lithostratigraphic and palynologic data of Cenozoic deposits of Tessik–Sarybulak depression. *In*: *Geology of Cenozoic and Seismotectonics of the Tien Shan (in Russian)*. Ilim, Bishkek, Kyrgyzstan, 26–39.

Gao, J. & Klemd, R. 2003. Formation of HP–LT rocks and their tectonic implications in the western Tianshan Orogen, NW China: geochemical and age constraints. *Lithos*, **66**, 1–22.

Gao, J., Zhang, L. & Liu, S. 2000. The 40Ar/39Ar age record of formation and uplift of the blueschists eclogites in the Western Tianshan Mountains. *Chinese Science Bulletin*, **45**, 1047–1051.

Gao, J., Long, L. *et al.* 2008. Tectonic evolution of the South Tianshan orogen and adjacent regions, NW China: geochemical and age constraints of granitoid rocks. *International Journal of Earth Sciences*, **98**, 1221–1238.

Glorie, S., De Grave, J., Buslov, M. M., Elburg, M. A., Stockli, D. F., Gerdes, A. & Van den haute, P. 2010. Multi-method chronometric constraints on the evolution of the Northern Kyrgyz Tien Shan granitoids (Central Asian Orogenic Belt): from emplacement to exhumation. *Journal of Asian Earth Sciences*, **38**, 131–146.

Glorie, S., De Grave, J. *et al.* 2011. Tectonic history of the Kyrgyz South Tien Shan (Atbashi-Inylchek) suture zone: the role of inherited structures during deformation-propagation. *Tectonics*, **30**, TC6016.

Guillot, S., Hattori, K., Agard, P., Schwartz, S. & Vidal, O. 2009. Exhumation processes in oceanic and continental subduction contexts: a review. *In*: Lallemand, S. & Funiciello, F. (eds) *Subduction Zone Geodynamics*. Frontiers in Earth Sciences. Springer, Berlin, 175–204.

Guo, J., Shu, L. S., Charvet, J., Laurent-Charvet, S. & Sun, S. 2002. Geochemical features of the two early palaeozoic ophiolitic zones and volcanic rocks in the Central-Southern Tianshan region, Xinjiang. *Chinese Journal of Geochemistry*, **21**, 308–321.

Hames, W. E. & Bowring, S. A. 1994. An empirical evaluation of the argon diffusion geometry in muscovite. *Earth and Planetary Science Letters*, **124**, 161–169.

Han, B. F., He, G. Q., Wang, X. C. & Guo, Z. J. 2011. Late Carboniferous collision between the Tarim and Kazakhstan–Yili terranes in the western segment of the South Tian Shan Orogen, Central Asia, and implications for the Northern Xinjiang, western China. *Earth-Science Reviews*, **109**, 74–93.

Handy, M. R., Schmid, S., Bousquet, R., Kissling, E. & Bernoulli, D. 2010. Reconciling plate-tectonic reconstructions of Alpine Tethys with the geological–geophysical record of spreading and subduction in the Alps. *Earth-Science Reviews*, **102**, 121–158.

Heermance, R. V., Chen, J., Burbank, D. W. & Miao, J. 2008. Temporal constraints and pulsed Late Cenozoic deformation during the structural disruption of the active Kashi foreland, northwest China. *Tectonics*, **27**, TC6012.

Hegner, E., Klemd, R. *et al.* 2010. Mineral ages and P-T conditions of Late Paleozoic high-pressure eclogite and provenance of mélange sediments from Atbashi in the south Tianshan orogen of Kyrgyzstan. *American Journal of Science*, **310**, 916–950.

Hendrix, M. S. 2000. Evolution of Mesozoic Sandstone Compositions, Southern Junggar, Northern Tarim, and Western Turpan Basins, Northwest China: a Detrital record of the Ancestral Tian Shan. *Journal of Sedimentary Research*, **70**, 520–532.

Hendrix, M. S., Graham, S. A., Carroll, A. R., Sobel, E. R., McKnight, C. L., Schulein, B. J. & Wang, Z. 1992. Sedimentary record and climatic implications of recurrent deformation in the Tian Shan: evidence from Mesozoic strata of the north Tarim, south Junggar, and

Turpan basins, northwest China. *Geological Society of America Bulletin*, **104**, 53–79.

HENDRIX, M. S., DUMITRU, T. A. & GRAHAM, S. A. 1994. Late Oligocene-early miocene unroofing in the Chinese Tian Shan: an early effect of the India-Asia collision. *Geology*, **22**, 487.

HOLLAND, T. J. B. 1980. The reaction albite = jadeite + quartz determined experimentally in the range 600–1200°C. *American Mineralogist*, **65**, 129–134.

HOLLAND, T. J. B. 1983. The experimental determination of activities in disordered and short-range ordered jadeitic pyroxenes. *Contributions to Mineralogy and Petrology*, **82**, 214–220.

HOLLAND, T. J. B. & BLUNDY, J. 1994. Non-ideal interactions in calcic amphiboles and their bearing on amphibole-plagioclase thermometry. *Contributions to Mineralogy and Petrology*, **116**, 433–447, http://doi.org/10.1007/BF00310910

HONGLIANG, W. 2007. *China Geological Map of the Tianshan and Adjacent Areas: 1:100 0000 (Chinese Edition)*. Geological Publishing House, China.

JIANG, C. Y., MU, Y. M., ZHAO, X. N., BAI, K. Y. & ZHANG, H. B. 2001. Petrology and geochemistry of active continental margin intrusive rock belt on the northern margin of the Tarim (in Chinese with english abstract). *Regional Geology of China*, **20**, 158–163.

JOLIVET, M. In press. Mesozoic tectonic and topographic evolution of Central Asia and Tibet: a preliminary synthesis. *In*: BRUNET, M.-F., MCCANN, T. & SOBEL, E. R. (eds) *Geological Evolution of Central Asian Basins and the Western Tien Shan Range*. Geological Society, London, Special Publications, **427**, http://doi.org/10.1144/SP427.2

JOLIVET, M., RITZ, J.-F. *ET AL.* 2007. Mongolian summits: an uplifted, flat, old but still preserved erosion surface. *Geology*, **35**, 871.

JOLIVET, M., DE BOISGROLLIER, T. *ET AL.* 2009. How old is the Baikal rift zone? Insight from apatite fission track thermochronology. *Tectonics*, **28**, TC3008.

JOLIVET, M., DOMINGUEZ, S., CHARREAU, J., CHEN, Y., LI, Y. & WANG, Q. 2010. Mesozoic and Cenozoic tectonic history of the central Chinese Tian Shan: reactivated tectonic structures and active deformation. *Tectonics*, **29**, 1–30.

KLEMD, R., BRÖCKER, M., HACKER, B. R., GAO, J., GANS, P. & WEMMER, K. 2005. New age constraints on the metamorphic evolution of the high-pressure/low-temperature belt in the Western Tianshan Mountains, NW China. *The Journal of Geology*, **113**, 157–168.

KONOPELKO, D., BISKE, G., SELTMANN, R., EKLUND, O. & BELYATSKY, B. 2007. Hercynian post-collisional A-type granites of the Kokshaal Range, Southern Tien Shan, Kyrgyzstan. *Lithos*, **97**, 140–160.

KONOPELKO, D., SELTMANN, R., BISKE, G., LEPEKHINA, E. & SERGEEV, S. 2009. Possible source dichotomy of contemporaneous post-collisional barren I-type versus tin-bearing A-type granites, lying on opposite sides of the South Tien Shan suture. *Ore Geology Reviews*, **35**, 206–216.

KONOPELKO, D., SELTMANN, R., APAYAROV, F., BELOUSOVA, E., IZOKH, A. & LEPEKHINA, E. 2013. U–Pb–Hf zircon study of two mylonitic granite complexes in the Talas-Fergana fault zone, Kyrgyzstan, and Ar–Ar age of deformations along the fault. *Journal of Asian Earth Sciences*, **73**, 334–346.

KRÖNER, A., KOVACH, V. *ET AL.* 2014. Reassessment of continental growth during the accretionary history of the Central Asian Orogenic Belt. *Gondwana Research*, **25**, 103–125.

LAGABRIELLE, Y. & CANNAT, M. 1990. Alpine Jurassic ophiolites resemble the modern central Atlantic basement. *Geology*, **18**, 319.

LANARI, P., GUILLOT, S., SCHWARTZ, S., VIDAL, O., TRICART, P., RIEL, N. & BEYSSAC, O. 2012. Diachronous evolution of the alpine continental subduction wedge: evidence from P–T estimates in the Briançonnais Zone houillère (France–Western Alps). *Journal of Geodynamics*, **56–57**, 39–54.

LANARI, P., RIEL, N., VIDAL, O. & HATTORI, K. H. 2013. Deciphering High-Pressure metamorphism in collisional context using microprobe-mapping methods: application to the Stak eclogitic massif. *Geology*, **41**, 111–114.

LANARI, P., ROLLAND, Y., SCHWARTZ, S., VIDAL, O., GUILLOT, S., TRICART, P. & DUMONT, T. 2014. P-T-t estimation of deformation in low-grade quartz-feldspar-bearing rocks using thermodynamic modelling and 40 Ar/39 Ar dating techniques: example of the Plan-de-Phasy shear zone unit (Briançonnais Zone, Western Alps). *Terra Nova*, **26**, 130–138.

LAURENT-CHARVET, S. 2001. *Accrétions Continentales en Asie Centro-Orientale: Évolution Géodynamique et Structurale du Tianshan et du Junggar Oriental (nord-ouest Chine) au Paléozoïque*. University of Orléans, France.

LI, Q., LIU, S., WANG, Z., HAN, B., SHU, G. & WANG, T. 2008. Electron microprobe monazite geochronological constraints on the Late Palaeozoic tectonothermal evolution in the Chinese Tianshan. *Journal of the Geological Society, London*, **165**, 511–522, http://doi.org/10.1144/0016-76492007-077

LI, Q., LIN, W., SU, W., LI, X., SHI, Y., LIU, Y. & TANG, G. 2011. SIMS U–Pb rutile age of low-temperature eclogites from southwestern Chinese Tianshan, NW China. *Lithos*, **122**, 76–86.

LI, Z., SONG, W., PENG, S., WANG, D. & ZHANG, Z. 2004. Mesozoic–Cenozoic tectonic relationships between the Kuqa subbasin and Tian Shan, northwest China: constraints from depositional records. *Sedimentary Geology*, **172**, 223–249.

LI, Z., ROECKER, S., ZHIHAI, L., BIN, W., HAITAO, W., SCHELOCHKOV, G. & BRAGIN, V. 2009. Tomographic image of the crust and upper mantle beneath the western Tien Shan from the MANAS broadband deployment: possible evidence for lithospheric delamination. *Tectonophysics*, **477**, 49–57.

LIN, W., FAURE, M., NOMADE, S., SHANG, Q. & RENNE, P. R. 2008. Permian–Triassic amalgamation of Asia: insights from Northeast China sutures and their place in the final collision of North China and Siberia. *Comptes Rendus Geoscience*, **340**, 190–201.

LIN, W., FAURE, M., SHI, Y., WANG, Q. & LI, Z. 2009. Palaeozoic tectonics of the south-western Chinese Tianshan: new insights from a structural study of the high-pressure/low-temperature metamorphic belt. *International Journal of Earth Sciences*, **98**, 1259–1274.

LIN, W., CHU, Y. *ET AL.* 2013. Geochronological and geochemical constraints for a middle Paleozoic continental arc on the northern margin of the Tarim block: implications for the Paleozoic tectonic evolution of the South Chinese Tianshan. *Lithosphere*, **5**, 355–381.

LIU, X., SU, W., GAO, J., LI, J., JIANG, T., ZHANG, X. & GE, X. 2014. Paleozoic subduction erosion involving accretionary wedge sediments in the South Tianshan Orogen: evidence from geochronological and geochemical studies on eclogites and their host metasediments. *Lithos*, **210–211**, 89–110.

LOMIZE, M. G., DEMINA, L. I. & ZARSHCHICOV, A. V. 1997. The Kyrgyz-Terskei Paleoceanic Basin, Tien Shan. *Geotectonics*, **31**, 463–482.

LOURY, C., ROLLAND, Y., GUILLOT, S., LANARI, P., ALEXEIEV, D. V. & MIKOLAICHUK, A. V. 2013. Geodynamic significance of preserved Carboniferous subduction complex in Atbashi Range (South Tianshan, Kyrgyzstan) and inferences for crustal-scale structure of north Tarim–Tibet orogenic system. *Journal of Nepal Geological Society*, **45**, 29.

LÜ, Z., ZHANG, L., DU, J. & BUCHER, K. 2008. Coesite inclusions in garnet from eclogitic rocks in western Tianshan, northwest China: convincing proof of UHP metamorphism. *American Mineralogist*, **93**, 1845–1850.

LÜ, Z., ZHANG, L. F., DU, J. X. & BUCHER, K. 2009. Petrology of coesite-bearing eclogite from Habutengsu Valley, western Tianshan, NW China and its tectonometamorphic implication. *Journal of Metamorphic Geology*, **27**, 773–787.

LÜ, Z., ZHANG, L., DU, J., YANG, X., TIAN, Z. & XIA, B. 2012. Petrology of HP metamorphic veins in coesite-bearing eclogite from western Tianshan, China: fluid processes and elemental mobility during exhumation in a cold subduction zone. *Lithos*, **136–139**, 168–186.

MA, H. F. 2002. Zonation characteristics of gold mineralization in eastern part of southern Tianshan and prospect prognosis (in Chinese with english abstract). *Uranium Geology*, **18**, 282–286.

MA, X., SHU, L., MEERT, J. G. & LI, J. 2014. The Paleozoic evolution of Central Tianshan: geochemical and geochronological evidence. *Gondwana Research*, **25**, 797–819.

MACAULAY, E. A., SOBEL, E. R., MIKOLAICHUK, A., LANDGRAF, A., KOHN, B. & STUART, F. 2013. Thermochronologic insight into late Cenozoic deformation in the basement-cored Terskey Range, Kyrgyz Tien Shan. *Tectonics*, **32**, 487–500.

MACAULAY, E. a., SOBEL, E. R., MIKOLAICHUK, A., KOHN, B. & STUART, F. 2014. Cenozoic deformation and exhumation history of the Central Kyrgyz Tien Shan. *Tectonics*, **33**, 135–165.

MAKAROV, V. I., ALEKSEEV, D. V. *ET AL.* 2010. Underthrusting of Tarim beneath the Tien Shan and deep structure of their junction zone: main results of seismic experiment along MANAS Profile Kashgar-Song-Köl. *Geotectonics*, **44**, 102–126.

METCALFE, I. 2013. Gondwana dispersion and Asian accretion: tectonic and palaeogeographic evolution of eastern Tethys. *Journal of Asian Earth Sciences*, **66**, 1–33.

METELKIN, D. V., GORDIENKO, I. V. & KLIMUK, V. S. 2007. Paleomagnetism of Upper Jurassic basalts from Transbaikalia: new data on the time of closure of the Mongol-Okhotsk Ocean and Mesozoic intraplate tectonics of Central Asia. *Russian Geology and Geophysics*, **48**, 825–834.

MEZGER, K., ESSENE, E. J. & HALLIDAY, A. N. 1992. Closure temperatures of the Sm—Nd system in metamorphic garnets. *Earth and Planetary Science Letters*, **113**, 397–409.

MIKOLAICHUK, A. V. & BUCHROITHNER, M. 2008. *Quaternary Removed Geological Map of the Khan Tengri Massif (ISTC project #KR-920) (1:200 000)*. Kyrgyz–Russian Slavic University, International Science and Technology Centre, Bishkek, Kyrgyzstan.

MIKOLAICHUK, A. V., KOTOV, V. V. & KUZIKOV, S. I. 1995. Structural position of the Malyi Naryn metamorphic complex as related to the problem of the boundary between the North and Median Tien Shan Geologic Structure of the Saru-Kungei Area. *Geotectonics*, **29**, 157–166 (English translation).

MIKOLAICHUK, A. V., KURENKOV, S. A., DEGTYAREV, K. E. & RUBSTOV, V. I. 1997. Northern Tianshan, main stages of geodynamic evolution in the late Precambrien and early Paleozoic. *Geotectonics*, **31**, 445–462.

MOLNAR, P. & TAPPONNIER, P. 1975. Cenozoic tectonics of Asia: effects of a continental collision. *Science*, **189**, 419–426.

NEWTON, R. C. 1992. An overview of charnockite. *Precambrian Research*, **55**, 399–405.

PORSHNYAKOV, G. S. 1983. *Geotectonics of the Tien Sahn and Pamirs Regions*. Nauka, Moscow (in Russian).

RAVNA, E. J. 2000. The garnet–clinopyroxene Fe^{2+}–Mg geothermometer: an updated calibration. *Science*, **18**, 211–219.

ROBBINS, G. 1972. *Radiogenic Argon Diffusion in Muscovite under Hydrothermal Conditions*. Brown University, Providencen RI.

ROLLAND, Y., ALEXEIEV, D. V., KRÖNER, A., CORSINI, M., LOURY, C. & MONIÉ, P. 2013. Late Palaeozoic to Mesozoic kinematic history of Talas-Ferghana strike-slip Fault (Kyrgyz West Tianshan) revealed by a structural study and 40Ar/39Ar dating. *Journal of Asian Earth Sciences*, **67–68**, 76–92.

SENGÖR, A. M. C., NATALIN, B. A. & BURTMAN, V. S. 1993. Evolution of the Altaid tectonic collage and Palaeozoic crustal growth in Eurasia. *Nature*, **364**, 299–307.

SHU, L., CHARVET, J., LINGZHI, G., LU, H. & LAURENT-CHARVET, S. 1999. A Large-scale Palaeozoic Dextral Ductile Strike-Slip Zone: the Aqqikkudug-Weiya Zone along the Northern Margin of the Central Tianshan Belt, Xinjiang, NW China. *Acta Geologica Sinica*, **73**, 148–162.

SIMONOV, V. A., SAKIEV, K. S., VOLKOVA, N. I., STUPAKOV, S. I. & TRAVIN, A. V. 2008. Conditions of formation of the Atbashi Ridge eclogites (South Tien Shan). *Russian Geology and Geophysics*, **49**, 803–815.

SOBEL, E. R. 1999. Basin analysis of the Jurassic–Lower Cretaceous southwest Tarim basin, northwest China. *Geological Society of America Bulletin*, **111**, 709–724.

SOBEL, E. R. & DUMITRU, T. A. 1997. Thrusting and exhumation around the margins of the western Tarim basin

during the India-Asia collision. *Journal of Geophysical Research*, **102**, 5043.

SOBEL, E. R., CHEN, J. & HEERMANCE, R. V. 2006*a*. Late Oligocene–Early Miocene initiation of shortening in the Southwestern Chinese Tian Shan: implications for Neogene shortening rate variations. *Earth and Planetary Science Letters*, **247**, 70–81.

SOBEL, E. R., OSKIN, M., BURBANK, D. & MIKOLAICHUK, A. 2006*b*. Exhumation of basement-cored uplifts: example of the Kyrgyz Range quantified with apatite fission track thermochronology. *Tectonics*, **25**.

SONG, X., CHEN, L., DENG, Y. & XIE, W. E. I. 2013. Syn-collisional tholeiitic magmatism induced by asthenosphere upwelling owing to slab detachment at the southern margin of the Central Asian Orogenic Belt. *Journal of the Geological Society, London*, **170**, 941–950, http://doi.org/10.1144/jgs2012-130

STERN, R. J., REAGAN, M., ISHIZUKA, O., OHARA, Y. & WHATTAM, S. 2012. To understand subduction initiation, study forearc crust: to understand forearc crust, study ophiolites. *Lithosphere*, **4**, 469–483.

SU, W., GAO, J. *ET AL*. 2010. U–Pb zircon geochronology of Tianshan eclogites in NW China: implication for the collision between the Yili and Tarim blocks of the southwestern Altaids. *European Journal of Mineralogy*, **22**, 473–478.

SUN, S. & MCDONOUGH, W. F. 1989. Magmatism in the ocean basins. *In*: SAUNDERS, A. D. & NORRY, M. J. (eds) *Geological Society London*. Geological Society, London, Special Publications, **42**, 313–345, http://doi.org/10.1144/GSL.SP.1989.042.01.19

TAGIRI, M., YANO, T., BAKIROV, A. A., NAKAJIMA, T. & UCHIUMI, S. 1995. Mineral paragenesis and metamorphic P-T paths of ultra-high pressure eclogites from Kyrghyzstan Tien-Shan. *The Island Arc*, **4**, 280–292.

TIAN, Z. L. & WEI, C. J. 2013. Metamorphism of ultrahigh-pressure eclogites from the Kebuerte Valley, South Tianshan, NW China: phase equilibria and P-T path. *Journal of Metamorphic Geology*, **31**, 281–300.

TURSUNGAZIEV, B. T. & PETROV, O. V. 2008. *Geological Map of Kirghyz Republic, Scale 1:500 000*. VSEGEI, St-Petersburg (in Russian).

VASSALLO, R., JOLIVET, M. *ET AL*. 2007. Uplift age and rates of the Gurvan Bogd system (Gobi-Altay) by apatite fission track analysis. *Earth and Planetary Science Letters*, **259**, 333–346.

VOGT, K. & GERYA, T. V. 2014. From oceanic plateaus to allochthonous terranes: numerical modelling. *Gondwana Research*, **25**, 494–508.

WANG, B., SHU, L. S., CLUZEL, D., FAURE, M. & CHARVET, J. 2007. Geochemical constraints on carboniferous volcanic rocks of the Yili Block (Xinjiang, NW China): implication for the tectonic evolution of Western Tianshan. *Journal of Asian Earth Sciences*, **29**, 148–159.

WANG, B., FAURE, M., SHU, L., CLUZEL, D., CHARVET, J., DE JONG, K. & CHEN, Y. 2008. Paleozoic tectonic evolution of the Yili Block, western Chinese Tianshan. *Bulletin de la Societe Geologique de France*, **179**, 483–490.

WANG, B., CLUZEL, D. *ET AL*. 2009. Evolution of calc-alkaline to alkaline magmatism through Carboniferous convergence to Permian transcurrent tectonics, western Chinese Tianshan. *International Journal of Earth Sciences*, **98**, 1275–1298.

WANG, B., LIN, W., CHARVET, J., FAURE, M., SHU, L. & CLUZEL, D. 2010. Guidebook for the international geological excursion in the Paleozoic chinese Tianshan. *Episodes*, **33**, 247–266.

WANG, B., SHU, L. *ET AL*. 2011. Paleozoic tectonics of the southern Chinese Tianshan: insights from structural, chronological and geochemical studies of the Heiyingshan ophiolitic mélange (NW China). *Tectonophysics*, **497**, 85–104.

WANG, B., CLUZEL, D. *ET AL*. 2014. Late Paleozoic pre- and syn-kinematic plutons of the Kangguer–Huangshan Shear zone: inference on the tectonic evolution of the eastern Chinese north Tianshan. *American Journal of Science*, **314**, 43–79.

WANG, T. Y. & LIU, J. K. 1991. A preliminary investigation on formative phase and rifting of Tarim Basin. *In*: JIA, R. X. (ed.) *Research of Petroleum Geology of Northern Tarim Basin*. China University of Geoscience Press, Wuhan, China, 115–124.

WATERS, D. J. 1996. *The Garnet–Cpx–Phengite barometer. Recommended Calibration and Calculation Method*, updated 1 March 1996. http://www.earth.ox.ac.uk/~davewa/research/eclogites/ecbarcal.html

WATERS, D. J. & MARTIN, H. N. 1993. Geobarometry of phengite-bearing eclogites. *Terra Abstracts*, **5**, 410–411.

WEI, C., WANG, W., CLARKE, G. L., ZHANG, L. & SONG, S. 2009. Metamorphism of high/ultrahigh-pressure Pelitic-Felsic Schist in the South Tianshan Orogen, NW China: phase Equilibria and P-T Path. *Journal of Petrology*, **50**, 1973–1991.

WELLS, P. R. A. 1977. Pyroxene thermometry in simple and complex system. *Contributions to Mineralogy and Petrology*, **62**, 129–139.

WENDT, A. S., D'ARCO, P., GOFFÉ, B. & OBERHÄNSLI, R. 1993. Radial cracks around a-quartz inclusions in almandine: constraints on the metamorphic history of the Oman Mountains. *Earth and Planetary Science Letters*, **114**, 449–461.

WINDLEY, B. F., ALLEN, M. B., ZHANG, C., ZHAO, Z.-Y. & WANG, G.-R. 1990. Paleozoic accretion and Cenozoic redeformation of the Chinese Tien Shan Range, central Asia. *Geology*, **18**, 128.

WINDLEY, B. F., ALEXEIEV, D. V., XIAO, W., KRÖNER, A., BADARCH, G. & KRONER, A. 2007. Tectonic models for accretion of the Central Asian Orogenic Belt. *Journal of the Geological Society, London*, **164**, 31–47, http://doi.org/10.1144/0016-76492006-022

XIAO, W.-J. 2004. Paleozoic accretionary and collisional tectonics of the eastern Tianshan (China): implications for the continental growth of central Asia. *American Journal of Science*, **304**, 370–395.

XIAO, W., WINDLEY, B. F., ALLEN, M. B. & HAN, C. 2013. Paleozoic multiple accretionary and collisional tectonics of the Chinese Tianshan orogenic collage. *Gondwana Research*, **23**, 1316–1341.

XIAO, X. C., TANG, Y. Q., FENG, Y. M., ZHU, B. Q., LI, J. Y. & ZHAO, M. 1992. *Tectonic Evolution of the Northern Xinjiang and its Adjacent Regions*. Geology pu., Beijing (in Chinese with English Abstract).

YANG, S. F., CHEN, H., JL, D., LI, Z., DONG, C., JIA, C. & WEI, G. 2005. Geological process of early to middle

Permian magmatism in Tarim Basin and its geodynamic significance (in Chinese). *Geology Journal of the China Universities*, **11**, 504–511.

YANG, S. F., LI, Z., CHEN, H., CHEN, W. & YU, X. 2006. 40Ar-39Ar dating of basalts from Tarim Basin, NW China and its implication to a Permian thermal tectonic event. *Journal of Zhejiang University Science A*, **7**, 320–324.

YANG, S. F., LI, Z. L., CHEN, H. L., SANTOSH, M. & YU, X. 2007. Discovery of Permian bimodal dyke: geochemistry and implications for tectonic evolution related to the last major tectono-thermal event in Tarim Basin, NW China. *Gondwana Research*, **12**, 113–120.

YANG, S. F., CHEN, H., LI, Z., LI, Y., YU, X., LI, D. & MENG, L. 2013. Early Permian Tarim Large Igneous Province in northwest China. *Science China Earth Sciences*, **56**, 2015–2026, http://doi.org/10.1007/s11430-013-4653-y.

YANG, T. N., LI, J. Y., SUN, G. H. & WANG, Y. B. 2006. Earlier devonian active continental arc in Central Tianshan: evidence of geochemical analyses and zircon SHRIMP dating on mylonitized granitic rocks (in Chinese with english abstract). *Acta Geologica Sinica*, **22**, 41–48.

YANG, X., ZHANG, L. F., GOU, L. L. & TIAN, Z. L. 2011. Petrology of coesite-bearing tourmaline–garnet–phengite schist from the Keburt Valley, western Tianshan, NW China. *Paper presented at the 9th International Eclogite Conference*. Marianske Lazne, Czech Republic.

YIN, A. & HARRISON, T. M. 2000. Geologic evolution of the Himalayan-Tibetan orogen. *Annual Review of Earth and Planetary Sciences*, **28**, 211–280.

YIN, A., NIE, S., CRAIG, P., HARRISON, T. M., RYERSON, F. J., XIANGLIN, Q. & GENG, Y. 1998. Late Cenozoic tectonic evolution of the southern Chinese Tian Shan. *Tectonics*, **17**, 1–27.

YU, X. 2009. *Magma Evolution and Deep Geological Processes of Early Permian Tarim Large Igneous Province (in Chinese)*. Zhejiang University, Hangzhou.

YU, X., YANG, S.-F., CHEN, H.-L., CHEN, Z.-Q., LI, Z.-L., BATT, G. E. & LI, Y.-Q. 2011. Permian flood basalts from the Tarim Basin, Northwest China: SHRIMP zircon U–Pb dating and geochemical characteristics. *Gondwana Research*, **20**, 485–497.

ZHANG, C.-L. & ZOU, H. 2013. Comparison between the Permian mafic dykes in Tarim and the western part of Central Asian Orogenic Belt (CAOB), NW China: implications for two mantle domains of the Permian Tarim Large Igneous Province. *Lithos*, **174**, 15–27.

ZHANG, L., AI, Y. *ET AL.* 2007. Triassic collision of western Tianshan orogenic belt, China: evidence from SHRIMP U–Pb dating of zircon from HP/UHP eclogitic rocks. *Lithos*, **96**, 266–280.

ZHANG, L. F., DU, J. X., SHEN, X. J., LÜ, Z., SONG, S. G. & WEI, C. J. 2009. The timing of UHP–HP eclogitic rocks in Western Tianshan, NW China: the new SIMS U–Pb zircon dating, Lu?Hf and Sm ?Nd isochron ages. *Paper presented at the 8th International Eclogite Conference. Qinghai province, China, 25 August to 3 September, 2009*.

ZHANG, Y., LIU, J. & GUO, Z. 2010. Permian basaltic rocks in the Tarim basin, NW China: implications for plume–lithosphere interaction. *Gondwana Research*, **18**, 596–610.

ZHAO, Z., ZHANG, Z., SANTOSH, M., HUANG, H., CHENG, Z. & YE, J. 2015. Early Paleozoic magmatic record from the northern margin of the Tarim Craton: further insights on the evolution of the Central Asian Orogenic Belt. *Gondwana Research*, **28**, 328–347.

ZHOU, D. W., SU, L. & JIAN, P. 2004. Zircon U-Pb SHRIMP ages of Yushugou ophiolitic terrane in Southern Tianshan and their tectonic implications. *Chinese Science Bulletin*, **49**, 1415–1419.

ZHOU, M.-F., ZHAO, J.-H., JIANG, C.-Y., GAO, J.-F., WANG, W. & YANG, S.-H. 2009. OIB-like, heterogeneous mantle sources of Permian basaltic magmatism in the western Tarim Basin, NW China: implications for a possible Permian large igneous province. *Lithos*, **113**, 583–594.